Micro-Engineered Devices for Point-of-Care Blood Clot Retraction Testing

by

Zida Li

A dissertation submitted in partial fulfillment
of the requirements for the degree of
Doctor of Philosophy
(Mechanical Engineering)
in the University of Michigan
2018

Doctoral Committee:

Associate Professor Jianping Fu, Chair
Professor Katsuo Kurabayashi
Assistant Professor Xiaogan Liang
Professor Kevin R. Ward

NANO MICRO
small

Clot Retraction

Whole blood coagulation testing provides valuable diagnostic information on diseases such as bleeding disorders, heart attack, deep venous thrombosis, etc. On page 3926, J. Fu and co-workers develop a miniaturized hemoretractometer to measure clot contraction upon blood coagulation with good reproducibility and robustness. This device design shows great application potential in point-of-care testing. Photo credit: David Peyer from University of Michigan.

29/2016
WILEY-VCH

A Miniaturized Hemoretractometer for Blood Clot Retraction Testing
J. Fu and co-workers

Zida Li

zidali@umich.edu

ORCID iD: 0000-0002-1353-9414

ACKNOWLEDGEMENTS

This thesis would not be possible without the help from a number of people.

I would like to thank my advisor, Prof. Jianping Fu, for his continuous support and guidance on my research. Prof. Fu has great passion in research and deep knowledge in both micro/nano engineering and cell biology. It has been my privilege to work with Prof. Fu on my PhD study and his constant advice has been instrumental to my development. As a supervisor, Prof. Fu has unique education philosophies and management style. Prof. Fu has great trust in his students, advising in a hands-off manner. It offered me the freedom to explore my research interests in various directions, such as microfluidics, nanomaterials, stem cell biology, and microengineered medical devices. It also offered me the opportunity to acquire knowledge in various subjects systematically. Prof. Fu has extraordinary working efficiency. His quick response on manuscript and proposal editing, as well as on administrative matters, significantly accelerated the research progress.

I would also like to thank my previous advisor, Prof. Anderson Ho Cheung Shum from the University of Hong Kong, with whom I worked for a year before my PhD. It was a blessing to work with Prof. Shum and working with him was very enjoyable and productive. His wisdom, passion, and kindness kept inspiring me to become a better researcher as well as a better person.

I would like to thank my other mentors at UM, especially Profs. Kevin Ward, Katsuo Kurabayashi, Xiaogan Liang, Allen Liu, and Nicholas Chronis, for their kind sharing of laboratory equipment, and most importantly, their insightful suggestions

on my research.

I would like to thank the Department of Mechanical Engineering, Coulter Translational Research Partnership Program, and National Institute of Health for providing the financial support for my thesis study.

I would like to thank my fellow lab mates and other research friends, including Dr. Koh Meng Aw Yong, Dr. Zeta Yu, Dr. Weiqiang Chen, Dr. Yubing Sun, Dr. Yue Shao, Dr. Shinuo Weng, Dr. Yi Zheng, Xiang Li, Jianming Sang, Ping Zhang, Xufeng Xue, Yuanyuan Zheng, Feng Lin, Chun-Yen Sung, Sajedeh Esfahani, Agnes Resto Irizarry, Sicong Wang, Yize Wang, Yujing Song, Meng-Ting Chung, Kenneth Kwun Yin Ho, Dr. Johanna Heureaux, Dr. Shue Wang, Dr. Luciana Kauer Rosselli-Murai, Jin Woo Lee, Brendan McCracken, Dr. Yang Song, Da Li, et al.. Their encouragements, suggestions, and company have played a tremendous role in keeping me moving forward. Conversations with Koh Meng, Yue, and Yi have been particularly enlightening, not only in addressing research obstacles, but also in making wiser life decisions.

Living abroad is not easy; doing a PhD abroad is even so. I am grateful to have all the friendships from various other communities besides research. I would like to thank my USTC fellows, especially Yawei Chen, my other friends at UM, especially Dr. Cesar Barraza and Kurt Lundeen, my fellow house mates at the North Campus Co-operative House (Escher House), especially Marc Gutierrez, Sameer Tammana, and Prof. Andrej Perdih, and many more. I am grateful for all the great time that I have spent with them, all the help that I have received from them, and everything I have learnt from them. Particularly, I learnt a tremendous amount of knowledge of English language and American culture from Marc, Sameer, and Kurt, which made my life in the U.S. much easier.

Finally, I would like to thank my parents, LI Yongzi and WEI Shuling, for their unreserved love, trust, and support. Thank them for granting me the freedom of

making my own life decisions without imposing their opinions on me. Thank them for exempting me from family responsibilities so that I can focus on my PhD study. Thank them for always encouraging me and caring about me so that I know there are always people whom I can hold on to. Something unfortunate happened during these five years, and unfortunately I was not able to be there when they needed me the most. I hope they stay happy and healthy, and I hope I will take better care of them in future.

TABLE OF CONTENTS

LIST OF FIGURES

Figure

LIST OF APPENDICES

Appendix

ABSTRACT

Blood coagulation is a critical hemostatic process that must be properly regulated to maintain the delicate balance between bleeding and clotting. Disorders of blood coagulation can expose patients to the risk of either bleeding disorders or thrombotic diseases. Coagulation diagnostics using whole blood is promising for the assessment of the complexity of the coagulation system and for global measurements of hemostasis. Despite the clinical values that existing whole blood coagulation tests have demonstrated, these systems have significant limitations that compromise their potential for point-of-care applications. Device miniaturization using micro-technology has the potential to provide assays with low blood consumption and high accuracy. However, the reported works either focused on developing tools for mechanistic study, or were complicated to be implemented for point-of-care applications.

This thesis aimed to leverage advances in micro-technology and functional soft materials to develop miniaturized devices for clot retraction force measurements, providing accurate and reliable blood coagulation assays with potentials for point-of-care applications.

First, I designed a force-sensing device, named Miniaturized Hemoretractometer (mHRM), based on image acquisition and analysis to measure the contraction force generated during blood clotting. This clot retraction force served as an indicator of coagulation functionality. I demonstrated that mHRM generated measurements that were consistent with reported works, under various conditions such as different temperatures and pro-/anti-coagulant treatments, which proved the efficacy of the

concept of using mHRM as a tool for blood coagulation diagnostics.

Acquiring electrical signals instead of images could vastly miniaturize the instrumentation of mHRM. However, integrating conductive materials into soft elastomer, such as PDMS, was a challenge. To address this problem, I developed a method to coat carbon nanotubes (CNTs) on PDMS surface from CNT solutions leveraging capillary action. I demonstrated that the deposited CNT films had good uniformity and piezoresistivity, making them strong candidate for the development of strain sensors. This study contributed a novel and convenient method for solution-based CNT deposition.

Finally, I applied this CNT deposition method into the design of mHRM and developed a CNT-strain-sensor-based mHRM (CNT-mHRM). I investigated the parameters that affected the sensitivity of CNT-mHRM devices and demonstrated that CNT-mHRM generated results that were consistent with image-analysis-based measurements. The utility of CNT-mHRM was further demonstrated by showing its capability of differentiating blood samples under pro- and anti-coagulation treatments. Thus, I have demonstrated the potential of CNT-mHRM devices as a practical point-of-care tool for blood coagulation diagnostics.

CHAPTER I

Introduction

This chapter is in part adapted from:

> Li, Zida, Xiang Li, Brendan McCracken, Yue Shao, Kevin Ward, and Jianping Fu. "A miniaturized hemoretractometer for blood clot retraction testing." *Small* 12, no. 29 (2016): 3926-3934.
>
> Li, Xiang, Weiqiang Chen, Zida Li, Ling Li, Hongchen Gu, and Jianping Fu. "Emerging microengineered tools for functional analysis and phenotyping of blood cells." *Trends in biotechnology* 32, no. 11 (2014): 586-594.

1.1 Background

1.1.1 Physiology of blood coagulation

Blood coagulation is a critical hemostatic process involving an intricate interplay between cellular (red blood cells, white blood cells, and platelets) and acellular components (plasma proteins) of the blood [1, 2]. It is normally initiated when the blood vessel is injured and the connective tissues (particularly collagen) underlying the endothelial lining of the vessel are exposed to blood flow, leading to platelet adhesion to connective tissues, activation, and aggregation, forming a plug at the site of vessel injury [3]. In the meanwhile, vessel injury also exposes tissue factors in connective

tissues to different coagulation factors in the blood plasma, ultimately leading to a coagulation cascade. The coagulation cascade involves the cleavage of fibrinogen, which then polymerizes into fibrin gel. Importantly, activated platelets bind and exert a contractile force on fibrin strands and promote the formation of a highly crosslinked fibrin network, which further strengthens the structural integrity of platelet plug, leading to increased clot strength and its elastic modulus [4, 5].

Among the various cellular and acellular components involved in blood coagulation, platelets, fibrinogen, and thrombin play particularly essential roles.

Platelets, or thrombocytes, are non-nucleated, discoid-shaped cell fragments, typically with a diameter of 2-4 µm and a thickness of about 0.5 µm [6]. They are generated when the cytoplasm of megakaryocytes in the bone marrow breaks up and enters the circulation [7]. Binding to connective tissue collagen stimulates platelets to release chemical agents, such as adenosine diphosphate and serotonin, leading to platelet activation. Upon activation, platelets undergo multiple changes in metabolism, shape, and surface proteins, which cause platelets to adhere to each other in a process called platelet aggregation, generating platelet plugs to seal small vessel breaks. Activated platelets also experience actomyosin-mediated muscle-like contraction, which improves the strength of platelet plugs and enhances the effectiveness in stopping bleeding. Platelet contraction is the direct source of clot retraction observed in coagulation assays.

Fibrinogen is a plasma glycoprotein composed of two trimers, with each composed of α, β, and γ chains [8]. During blood clotting, fibrinogen is cleaved to form individual fibrin strands and two small polypeptides, which are derived from alpha and beta chains. Individual fibrin strands polymerize to form fibrin network and provide the scaffold of blood clots. Additionally, fibrin binds to platelets through platelets' surface membrane receptors. At the end of blood clotting, the fibrin network is broken down in a process called fibrinolysis, primarily mediated by plasmin. Cross-linking

of fibrinogen leads to the viscoelasticity change of blood during clotting, which is the foundation of thromboelastography-based blood coagulation assays [9] discussed later.

Thrombin is a serine protease converted from plasma protein prothrombin in coagulation cascade. Thrombin catalyzes and stabilizes the formation of fibrin network from fibrinogen [10]. In addition, thrombin activates several coagulation factors, forming a positive feedback and promoting blood coagulation. Thrombin is also an important activator of platelets. Therefore, comprised function of thrombin has profound effect on blood coagulation. For example, heparin, a commonly used anticoagulant, prevents blood coagulation by activating protein antithrombin, which inhibits the activity of thrombin.

Besides these three participants, calcium is also essential to coagulation. Effective activation of coagulation factors relies on the binding of these factors to cell surfaces. This surface binding is dependent on calcium and, therefore, sequestering of calcium prevents blood from coagulating [11]. Though calcium concentration in the plasma can never be low enough to cause clotting defect before other fatal conditions occur, sequestering of calcium has been the mechanism of several commonly used anticoagulants, such as citrate and ethylenediaminetetraacetic acid (EDTA).

Blood coagulation must be properly regulated to maintain the delicate balance between bleeding and clotting. Disorders of blood coagulation can expose patients to the risk of either bleeding disorder, such as hemophilia and Glanzmann's thrombasthenia, or thrombotic diseases, such as heart attack, stroke, deep venous thrombosis, pulmonary embolism, etc.[12]. Therefore, the ability to accurately determine the hemostatic profile of a patient is of great importance for the diagnosis of clotting-related diseases.

In addition, monitoring of coagulation functionality is critical in making clinical decisions for many therapies, including hemostatic therapy [13], transfusion therapy

[14], and anticoagulation therapy. For example, in perioperative care, rapid and robust reporting of hemostatic profile provides critical information for the decision on anticoagulant dosage, which is important in minimizing the need of blood transfusion. Another example is the treatment of thrombotic diseases with anticoagulation therapy. Accurate profiling of coagulation functionality helps clinicians decide the optimal dosage of anticoagulant administration, reducing the risk of bleeding disorders and other complications.

1.1.2 Assays for coagulation functionality

Coagulation diagnostics using whole blood samples has been proposed as an effective method for assessing the complexity of the coagulation system and for global measurements of hemostasis. Compared to routine coagulation tests in the clinic (such as prothrombin time or PT, activated partial thromboplastin time or aPTT, and platelet count), whole-blood coagulation tests offer significant advantages of measuring the whole clotting process, starting with fibrin formation and continuing through to clot retraction and fibrinolysis, and allowing the plasmatic coagulation system to interact with blood cells including platelets, thereby providing useful additional information on platelet function [15]. Among different whole blood coagulation tests, viscoelastic hemostasis assays including thromboelastography (TEG) and rotational thromboelastometry (ROTEM) have gained significant attention in the clinic [16]. In principle, TEG and ROTEM measure the changes in the strength and elasticity of whole blood upon clotting. For example, TEG consists of a rotating cup and a pin which is connected to a rotation sensor. Blood sample is held in the cup and the pin is submerged in the blood sample during the assay. When the blood starts clotting, its viscoelasticity changes, leading the pin to rotate along with cup. The rotational amplitude of the pin is recorded by the rotation sensor and reported for analysis of the viscoelasticity change of the blood sample. Such viscoelastic hemostasis assays have

been shown to provide critical information on the interactivity of the major phases of clot formation and lysis and on the functional differences between different cellular and acellular components of the blood for differentiating the mechanism(s) related to clotting abnormalities [17].

Besides viscoelastic hemostasis assays, whole-blood clot retraction assays using devices such as Hemodyne Hemostasis Analysis System (HAS, Hemodyne, Inc.) are another method reported to provide important information on blood coagulation function, reporting on clot elastic modulus and platelet contractile force (or clot retraction force) [18, 19]. In HAS, whole blood samples are confined between two plates (either flat-flat or cone-cone surfaces), with the top plate attached to a strain-gauge transducer. Clotting of blood results in a downward force pulling the top plate, which is directly measured in real time by the strain-gauge transducer. Using HAS, clot retraction force has been shown to be sensitive to platelet count, platelet metabolic status, glycoprotein IIB/IIIa status, and the presence of antithrombin activities [18]. Importantly, clinical applications of the HAS have demonstrated promising applications of such whole blood clot retraction assays for rapid assessment of global hemostasis [20–22] and the response to a variety of procoagulant and anticoagulant medications [23–25].

Despite the clinical values that existing whole blood coagulation tests have demonstrated through initial applications, such systems still have significant limitations in terms of costly expense to make and repair, limited sample throughput, large footprint, and excessive sample size (> 0.3 mL) that can be problematic for repetitive assays on pediatric patients, inter-assay variability, and significant user interventions, rendering them suboptimal for point-of-care applications [26].

Device miniaturization based on emerging functional materials and micro/nanotechnology holds great potential to develop assays with low cost, low blood consumption, and high accuracy, which are suitable for point-of-care application. Several

works have been reported, and these works assessed either of the two important biophysical properties of blood clotting: viscoelasticity change and platelet contractile force dynamics.

Similar as TEG and ROTEM, the principle of measuring viscoelasticity using miniaturized devices is to apply actuation, commonly vibration, to blood samples and monitor the response over time. For example, in a study based on oscillating cantilever, the cantilever was actuated and the resultant oscillation of the cantilever was dependent on the viscoelasticity of the blood samples that the cantilever was merged in [27]. By monitoring the oscillation, blood viscoelasticity could be deduced. Another study used actuated surface-attached posts that were deformed under magnetic field; this deformation was dependent on the stiffness of the blood sample, which served as the measuring principle [28]. Similar concepts were also adopted in the studies using capillary flows [29, 30].

Several methods were developed to measure platelet contractile force. For example, traction force microscopy was employed to study the dynamic evolution of platelet contractile force during platelet activation, where microbeads were incorporated into the surface of a compliant polymer substrate and platelets were allowed to adhere and exert platelet contractile force on the substrate [31]. When the platelets started contracting, displacements of beads were observed and recorded to deduce the force field. Another successful cell traction force measurement tool, termed a micropost force sensor, was also utilized to measure platelet contractile force [32]. Platelets were seeded on top of polydimethylsiloxane (PDMS) microposts pre-coated with fibrinogen or fibronectin to facilitate platelet adhesion. Once platelets were activated by addition of thrombin, deflections of the microposts were observed and recorded to calculate platelet contractile force based on Euler–Bernoulli beam theory. Variations of this method have been developed to study the effects of glycoprotein Ib and von Willebrand factor (vWF) [33] and shear force [34] on platelet contraction.

In another recent study, custom-built side-view atomic force microscopy (AFM) was used to measure the platelet contractile force generated by single platelets bridging the AFM cantilever and a substrate [35].

These reported micro-engineered tools have significantly improved measurement accuracy and sensitivity to unprecedented levels. However, these tools were designed primarily for mechanistic studies and thus are complicated and suboptimal for direct clinical applications. Microengineered tools that are convenient for point-of-care blood coagulation assays remains to be developed.

1.2 Thesis objectives and outline

This thesis aims to leverage the advances in micro-technology and functional soft materials and develop a miniaturized device, named Miniaturized Hemoretractometer (mHRM), for accurate and reliable blood coagulation assay with potentials for point-of-care applications. In particular, I designed flexible beams with image analysis modules to measure the contraction force generated during blood clotting. This clot retraction force served as an indicator of coagulation functionality. To equip mHRM with real-time electrical readout, I developed a method to deposit piezoresistive material, namely carbon nanotube, on soft elastomer PDMS. Using this deposition technique, I fabricated piezoresistor strain sensors on the beams in mHRM and demonstrated its applicability.

The current chapter talks about the physiological background of blood coagulation and the significance of effective assays. It also talks about the limitations of existing assays, including conventional tools and emerging tools based on device miniaturization. The overall objective of this thesis is then discussed.

Chapter 2 describes the design, characterization, and validation of mHRM that is based on image analysis. Taking advantage of surface tension, this design adopted two beams with protrusions to hang a blood drop. Such design ensured reproducible

localization of blood samples after loading. Characterization was performed with finite element methods in COMSOL; the simulation model and results were discussed. mHRM devices were validated by testing blood samples using pig blood samples under varied conditions with known coagulation profiles, including different temperature, with and without coagulation activator, and pro-/anti-coagulant treatment. A comparison with standard tests TEG is also presented. Following these experimental results, the outlook of clinical application is discussed in detail.

Though mHRM showed potential in clinical applications for point-of-care blood coagulation testing, its data acquisition relied on image capturing and thus optical instruments. Further democratization of mHRM required replacement of image capturing with electrical signal acquisition in raw data collection, which could be achieved with a specially designed integrated circuits. However, integrating electrical units in PDMS has been a challenge.

Chapter 3 describes a method of depositing piezoresistive material, namely carbon nanotube (CNT), on PDMS surface. Micropillar arrays were fabricated on elastic PDMS substrates and then the PDMS surfaces were treated by oxygen plasma to render them hydrophilic. After CNT solution was dispensed onto the PDMS substrate, capillary force spread CNT solution evenly on the PDMS substrate. Water evaporation left a uniform deposition of CNT on PDMS substrates. The morphology of CNT is presented and the effect of CNT concentration and micropillar gap size on CNT coating uniformity, film conductivity, and piezoresistivity are discussed.

Chapter 4 discusses an improved mHRM by implementing the CNT deposition method into a new device design, named CNT-mHRM. In the new design, I adopted a fixed protrusion and a thin PDMS beam to localize the blood sample, and deposited CNT on the backside of PDMS beam to serve as the strain sensor. The design and fabrication of the device is discussed, and the characterization of electro-mechanical response is presented. The validity of the devices is demonstrated by the compari-

son of test results with those from image analysis, and the utility of the devices is demonstrated by showing CNT-mHRM's capability of differentiating blood samples with different coagulation profiles.

Chapter 5 summarizes this thesis work and discusses its potential application in commercialization as well as in laboratory research. Potential directions for further improvement on the device performance are also discussed.

CHAPTER II

The imaging-based hemoretractometer for blood clot retraction testing

This chapter is in part adapted from:

> Li, Zida, Xiang Li, Brendan McCracken, Yue Shao, Kevin Ward, and Jianping Fu. "A miniaturized hemoretractometer for blood clot retraction testing." *Small* 12, no. 29 (2016): 3926-3934.

2.1 Introduction

Blood coagulation is a critical hemostatic process that must be properly regulated to maintain a delicate balance between bleeding and clotting. Disorders of blood coagulation can expose patients to the risk of either bleeding disorders or thrombotic diseases. Coagulation diagnostics using whole blood is very promising for assessing the complexity of the coagulation system and for global measurements of hemostasis. Despite the clinic values that existing whole blood coagulation tests have demonstrated, these systems have significant limitations that diminish their potential for point-of-care applications. In this chapter, I leveraged recent advancements in small scale device fabrication using functional soft materials [36] and developed a miniaturized clot retraction assay device termed Miniaturized Hemoretractometer (mHRM).

In the mHRM, two doubly-clamped mechanical strain sensing beams (in millimeter size range) made with soft elastomer polydimethylsiloxane (PDMS) were utilized for holding prescribed minute amounts of blood samples while simultaneously measuring clot retraction force during blood clotting. Kinetic curves of clot retraction force obtained by the mHRM were utilized for analysis of different major phases of clot formation and extraction of key blood clotting parameters. Using mHRM, we further conducted whole blood coagulation assays to determine the effect of assay temperature, treatments of clotting agent, and pro- and anti-coagulant on clot retraction force development.

2.2 Experimental section

2.2.1 Device design and fabrication

The mHRM device consisted of three sandwiched layers, with the middle structural layer containing two parallel doubly-clamped beams as mechanical strain sensors to measure dynamic clot retraction force during blood clotting (Figure 2.1). In the mHRM, the structural layer was embedded between a top cover layer and a bottom support layer. Each strain sensing beam contained a protrusion in the middle of the beam to hold a prescribed minute blood sample. In this proof-of-concept device, positions of fiducial markers engraved onto the protrusions of the strain sensing beam were recorded using a camera during blood clotting assays for quantitative measurements of beam displacements.

All the three layers of the mHRM device were fabricated through replica molding of soft materials (Figure 2.2). Patterns of molds were first generated using AutoCAD (Autodesk, Inc.). A laser cutter was used to cut acrylic sheet (Inventables, Inc.) into desired patterns. These acrylic patterns were affixed to the bottom of a petri dish using double-sided tape before degassed polydimethylsiloxane (PDMS) prepolymer

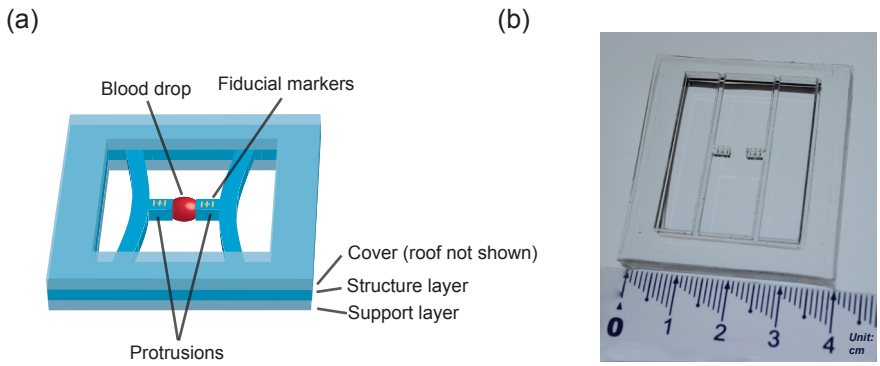

Figure 2.1: (a) Schematic of the mHRM. A structural layer containing two doubly-clamped force sensing beams was sandwiched between a top cover layer and a bottom support layer. Each force sensing beam contained a protrusion in the middle of the beam to hold whole blood samples. Positions of fiducial markers engraved onto the protrusions were recorded for quantitative measurements of beam displacements during blood clot formation. (b) Photograph of the mHRM device.

(10:1 base-to-curing agent ratio) was poured into the petri dish. The dish was placed in a 60 °C oven overnight, before PDMS was peeled off and cut into desired dimensions to form the top cover and bottom support layers of the mHRM device.

The structure layer of the mHRM device containing doubly-clamped strain sensing beams was fabricated using a double molding protocol. Briefly, an acrylic pattern was first cut by laser into the same shape as the final structural layer before being used as a mold to generate a negative mold using PDMS (10:1 base-to-curing agent ratio). Fiducial markers were generated by engraving the acrylic sheet before the sheet was used as a mold. After being cured and peeled off from the acrylic mold, the negative PDMS mold was activated with oxygen/air plasma (PDC-001, Harrick Plasma), followed by surface passivation with trichloro(1H,1H, 2H,2H-perfluorooctyl)silane (Sigma-Aldrich Co.), before degassed PDMS prepolymer (20:1 base-to-curing-agent ratio) was poured onto the mold and excess PDMS was removed using a razor blade. The negative PDMS mold was then placed in a 60 °C oven for 6 hr before the final structural layer was peeled off from the mold. The structural layer was briefly treated with air plasma

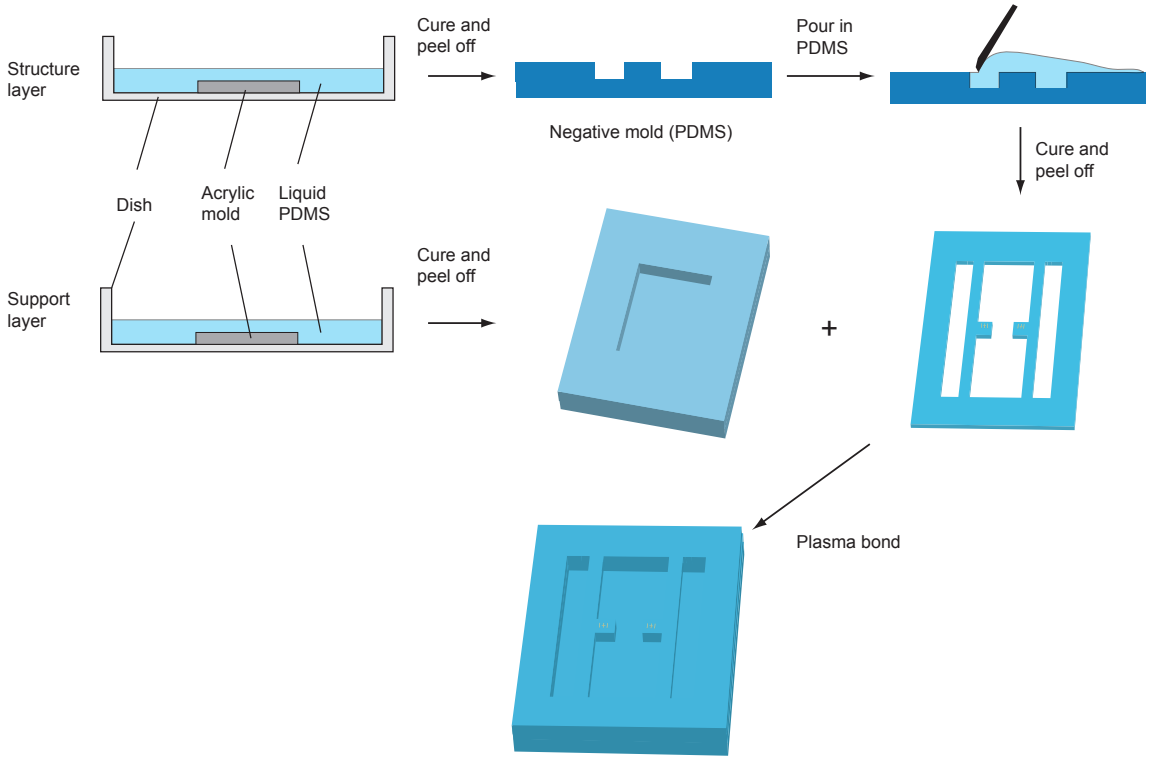

Figure 2.2: Fabrication of the mHRM device. The structure layer was fabricated by a double molding protocol. Laser-cut acrylic mold was affixed onto a dish before liquid PDMS prepolymer was poured in, which was then cured and peeled off to form the negative mold. Liquid PDMS prepolymer was then poured on the negative mold, with the excess PDMS being removed using a blade. After curing, the final structure layer was peeled off from the negative mold. Support layer was fabricated by single molding in a similar way. The structure and support layer were bonded together after surface activation with oxygen plasma.

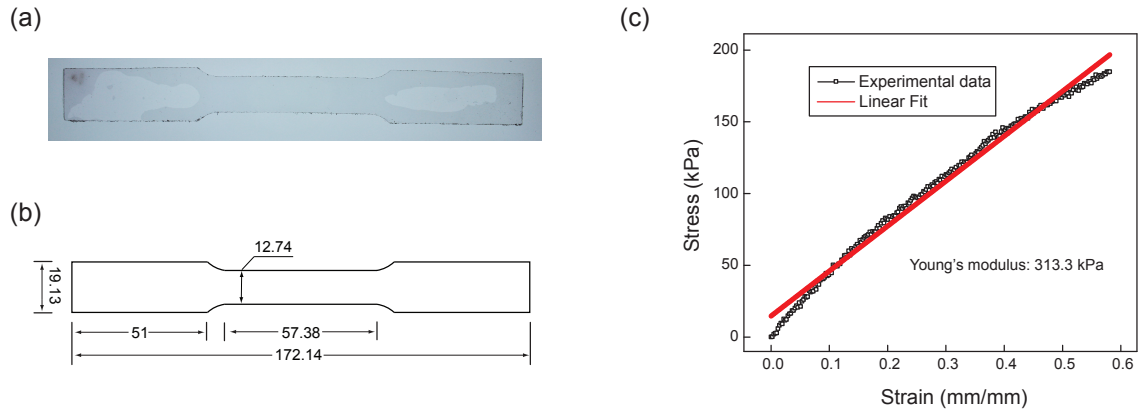

Figure 2.3: Tensile testing methods. (a,b) Testing specimen and dimensions. (Unit: mm) (c) Plotted stress-strain curve from the testing and the linear fit of strain-stress relation. The Young's modulus in this case was calculated to be 313.3 kPa.

before being bonded with the bottom support layer (Figure 2.1b).

The fabrication protocol was established to generate mHRM devices with consistent geometries (with standard deviations less than 4% of the mean; data not shown). The width, length, and thickness of the doubly-clamped PDMS strain sensing beams used in this work were 1.0 mm, 35.5 mm, and 2.0 mm, respectively. The millimeter size scale of the mHRM facilitates its assembly process. Success rate of mHRM fabrication was about 80%, with the cost of a single mHRM device estimated to be about 7 U.S. Dollars. We further used an Instron tensile testing machine (Norwood, MA) to calibrate the Young's modulus of PDMS prepared for the structural layer of the mHRM device (Young's modulus, ∼300 kPa; Figure 2.3).

2.2.2 FEM simulation

FEM simulation was performed in COMSOL Multiphysics (COMSOL, Inc.). Briefly, a stationary solid mechanics model was developed with a beam subjected to gravity ($g = 9.8$ m/s^2). A downward vertical force was uniformly exerted on the protrusion surface to mimic the effect of blood weight (70 µN). The Young's modulus, density, and Poisson's ratio of PDMS were 300 kPa, 970 kg/m^3, and 0.49, respectively. To

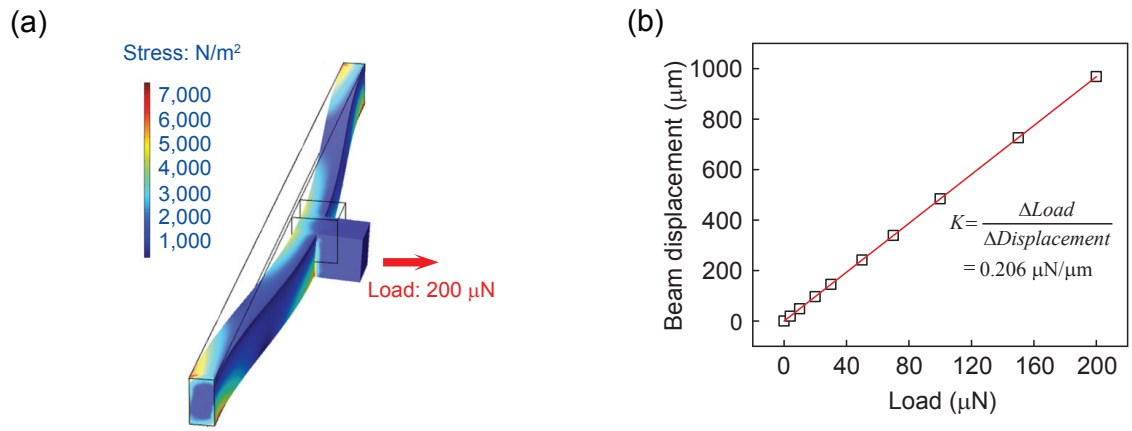

Figure 2.4: (a) FEM simulation of beam displacement showing stress distribution and beam deformation when a prescribed horizontal load of 200 μN was applied uniformly on the beam protrusion. (b) Beam displacement as a function of horizontal load. Linear fitting was used to determine the spring constant K of the force sensing beam.

simulate the effect of blood clotting and contraction on beam deformation, another horizontal load was applied uniformly on the protrusion (Figure 2.4a). Through FEM simulation, horizontal beam displacement was calculated as a function of horizontal load, linear fitting of which provided the effective spring constant K of the PDMS strain sensing beam ($K = 0.206$ μN/μm; Figure 2.4b), which would be used directly for calculation of clot retraction force in experiments by multiplying K with horizontal beam displacement. The spring constant K of the PDMS strain sensing beam was further validated using the classical beam theory following

$$K = 16E\delta W^3/L^3 \tag{2.1}$$

where E was the Young's modulus, and δ, W, and L were the beam thickness, width, and length, respectively. K was calculated to be 0.206 μN/μm.

2.2.3 Blood specimen and coagulation assays

Under a protocol approved by the University of Michigan's Committee on Care of Use of Animals, whole blood specimens were collected from healthy pigs into a vacutainer (BD Vacutainer, BD Company) containing 3.2% sodium citrate. All blood samples were assayed within 6 hr after blood collection.

Unless otherwise stated, all clot retraction force measurements were conducted using re-calcified whole blood without additional pre-treatment. Briefly, 12.75 µL citrated whole blood was suspended between the two protrusions of the PDMS strain sensing beams by pipetting, before another 0.75 µL $CaCl_2$ solution (0.2 M, Fisher Scientific) was added into the blood drop. For mixing, a pipette was inserted into the blood and stirred up gently. The top cover layer was then placed on top of the mHRM device, and image acquisition was started immediately using a microscope coupled with a digital camera (Dino-Lite Handheld Digital Microscope, AnMo Electronics Co.) at one or two frames per minute. To minimize blood evaporation, water drops were placed inside the mHRM device, and the surrounding area of the top cover layer was applied with PDMS prepolymer before being placed on the structural layer of the mHRM device. Coagulation assays at 37 °C were conducted in a stage-top incubation chamber (PM S1, Zeiss, Inc.). Assays at 25 °C were performed in a room equipped with a thermostat and air conditioning system.

To activate platelets and thus expedite clot retraction force development, 1 µL thrombin (100 U/mL, Cayman Chemical Company) was added into the blood as a clotting factor. To assay the effects of pro- and anti-coagulants on clot retraction force development, aprotinin (80 µg/mL; Sigma-Aldrich Co.) and heparin (8 U/mL; Sigma-Aldrich Co.) were further added into the blood in separate experiments. Drug treated blood samples were incubated at room temperature for one hour before loaded into the mHRM device for clot retraction force measurements.

Thromboelastography (TEG) was conducted using the TEG 5000 Thrombelas-

tograph Hemostasis Analyzer System (Haemonetics Corp., Braintree, MA) following standard protocols for citrated whole blood samples.

2.2.4 Image processing and data analysis

Images were processed via template matching using MATLAB (MathWorks, Inc.) to obtain displacement data of doubly-clamped PDMS strain sensing beams. Briefly, an area in the first image of the beam containing the fiducial markers was selected as the template, and each of the following images was analyzed to determine the best match of this template, the location of which was extracted for beam displacement analysis. Displacements of doubly-clamped strain sensing beams were then converted to clot retraction forces CRF using Hooke's law.

The data of clot retraction force during the contraction development phase was fitted using a quadratic function to obtain key coagulation parameters, including reaction time T_r, time to maximum amplitude T_{max}, CRF growth rate G_{CRF}, and maximum CRF CRF_{max}. Specifically, T_r was defined as the time when CRF started to increase from the baseline level ($CRF = 0$ µN), time to maximum amplitude T_max was the time it took for CRF to reach its maximum value CRF_{max}, and G_{CRF} was defined as the CRF growth rate at T_r ($G_{CRF} = dCRF/dT|_{T=T_r}$). Statistical analysis was conducted using Origin (OriginLab Corp.). Two-sample unpaired Student's t-test was performed, and only p-values less than 0.05 were considered statistically significant.

2.3 Results

2.3.1 mHRM device design and characterization

Design of the mHRM device incorporated two doubly-clamped PDMS beams with protrusions at the beam centers to hold blood samples (Figure 2.1). The doubly-

clamped PDMS beams served simultaneously as mechanical strain sensors to report clot retraction forces in real time during blood clotting, through direct measurements of positions of fiducial markers engraved onto the protrusions of PDMS strain sensing beams. A fabrication protocol was established to generate the mHRM device using replica molding of PDMS (see Experimental section; Figure 2.2), resulting in consistent and precise geometries of PDMS strain sensing beams and their distance, critical for precise measurements of clot retraction force. The width, length, and thickness of doubly-clamped PDMS strain sensing beams used in this work were 1.0 mm, 35.5 mm, and 2.0 mm, respectively. The Young's modulus of PDMS was further calibrated using a standard tensile testing protocol to be about 300 kPa (see Experimental section), consistent with previously published data [37]. We further conducted FEM simulations to determine the effective spring constant K of the doubly-clamped PDMS strain sensing beams ($K = 0.206$ µN/µm), which was then used directly for quantification of clot retraction force by multiplying K with beam displacement (Hooke's law; Figure 2.4). During blood coagulation assays, 12.75 µL citrated whole blood was suspended between the two protrusions of PDMS strain sensing beams by pipetting, before another 0.75 µL $CaCl_2$ solution (0.2 M) was added into the blood for re- calcification and initiation of blood clotting. In order to understand if PDMS surface has any intrinsic effect on blood coagulation, studies were undertaken in which we coated TEG cups (blood receptacles) with PDMS. Blood was then added and TEG measurements were performed. Results indicated that when compared to non-PDMS-coated controls, PDMS had no measureable effect on blood coagulation (Figure 2.5).

Figure 2.6 demonstrates a temporal series of representative bright field images showing clotting of a blood drop suspended between the two protrusions of PDMS strain sensing beams recorded using a digital camera immediately after blood re-calcification (designated as $T = 0$).

This blood coagulation assay was conducted at 25 °C, with 1 µL thrombin (100

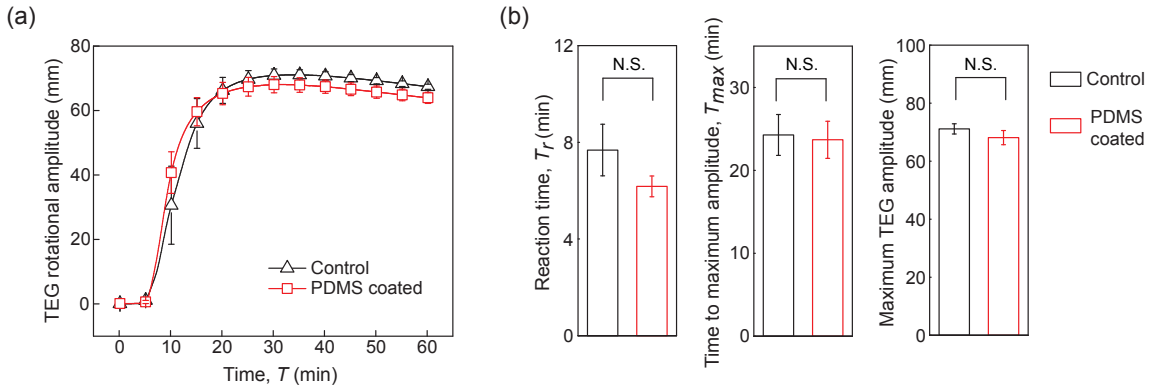

Figure 2.5: Effect of PDMS on blood coagulation. (a) Comparison of TEG tracings using regular TEG cups and cups pre-coated with PDMS. (b) Bar plots of reaction time T_r, time to maximum amplitude T_{max}, and maximum TEG amplitude as a function of PDMS coating. Data represents the mean ± SEM with n = 5. P-values were calculated using two-sample unpaired student t- test.

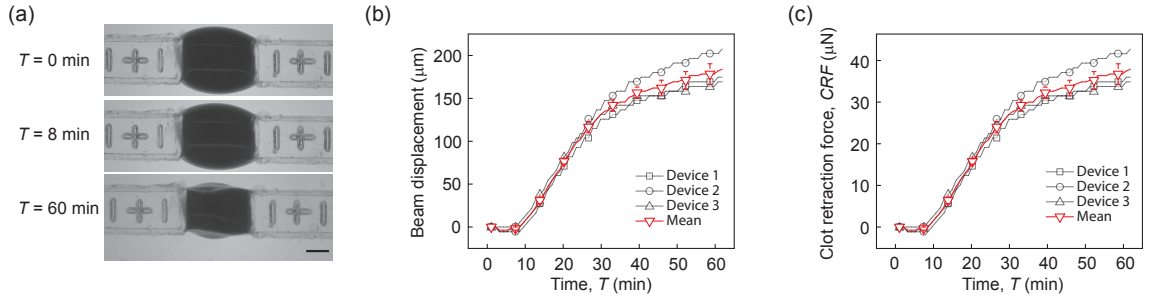

Figure 2.6: (a) Representative micrographs showing the dynamic process of blood clot formation at different time points. Blood clotting and contraction caused the two opposite force sensing beams to bend toward each other. Positions of fiducial markers were determined through image processing for quantitative measurements of beam displacements and thus clot retraction force CRF. Scale bar, 1 mm. (b) Beam displacement as a function of time, with t = 0 being the moment of thrombin and calcium addition (see Experimental section), for three different mHRM devices. Data represents the mean ± SEM. (c) Clot retraction force CRF calculated based on the spring constant K of the doubly-clamped force sensing beam and beam displacement.

U/mL) added into the blood prior to mHRM measurement. Thrombin, as a common clotting factor, is an important intermediate product of the blood coagulation process and cleaves fibrinogen to form fibrin networks. Thus, adding thrombin into blood can expedite the coagulation cascade in a positive feedback fashion. Importantly, thrombin also directly activates platelets and induces platelet contraction [38]. Imaging analysis was conducted to quantify displacement of fiducial markers (and thus strain sensing beams) as a function of time to determine dynamic clot retraction force CRF during blood clotting (Figure 2.6b & c). Data of PDMS strain sensing beam displacement and clot retraction force shown in Figure 2.6b & c were obtained from three separate coagulation assays using three different mHRM devices, suggesting consistent measurements and satisfactory reproducibility of the mHRM device for clot retraction force measurements (SEMs were generally around 6% of the mean CRF).

2.3.2 Dynamic clot retraction force development

Kinetic curves of clot retraction force obtained by the mHRM device helped reveal different major phases of clot formation (Figure 2.7), consistent with those revealed by TEG (Figure 2.8). In the first reaction phase between blood re-calcification ($T = 0$) and onset of clot retraction force development ($T = T_r$), clot retraction force was essentially zero and not detected by the mHRM (Figure 2.6b & c). In this reaction phase, the coagulation cascade was underway for formation of the fibrin network needed for clot retraction force development. Onset of clot retraction force development occurred as soon as the fibrin network was in place, and interactions between activated platelets and fibrin strands led to a rapid increase of clot retraction force and initiation of blood clot contraction ("the contraction development phase"; Figure 2.7). In the contraction development phase, clot retraction force CRF increased rapidly before approaching a plateau (CRF_{max}; Figure 2.7). We designated duration

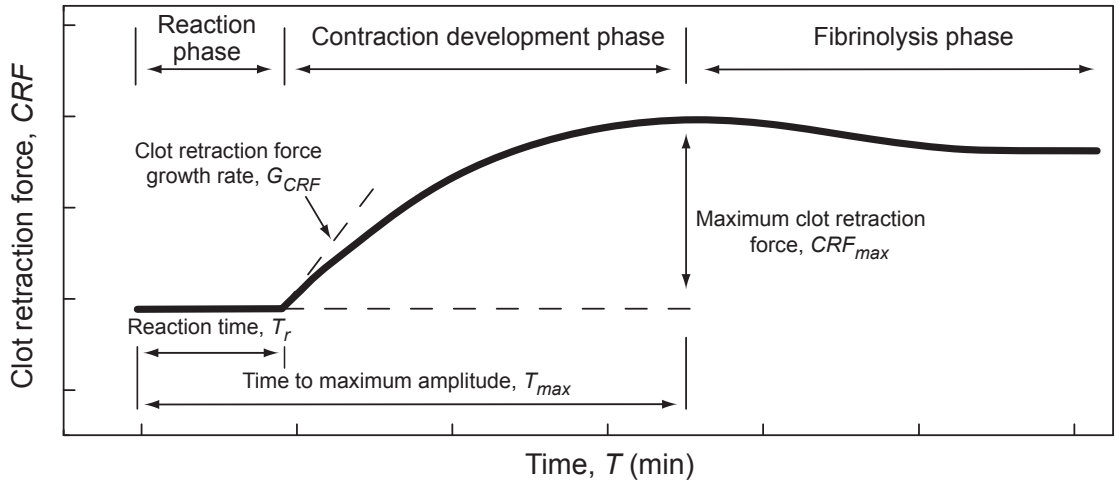

Figure 2.7: Schematic of dynamic evolution of the CRF during the whole blood coagulation process. Key parameters, including reaction time T_r, time to maximum amplitude T_{max}, CRF growth rate G_{CRF}, and maximum CRF CRF_{max}, were highlighted.

of the reaction phase as T_r and the time it took for clot retraction force to reach its maximum as T_{max}. Growth rate of clot retraction force G_{CRF} was defined as

$$G_{CRF} = \left.\frac{dCRF}{dT}\right|_{T=T_r} \tag{2.2}$$

Kinetic curves of clot retraction force measured by the mHRM further revealed a clot lysis phase immediately following the contraction development phase, similar to those observed in TEG. In the fibrinolysis phase, clot retraction force decreased slowly from the plateau value CRF_{max} due to fibrin network being disintegrated. Together, the reaction time T_r, time to maximum clot retraction force T_{max}, clot retraction force growth rate G_{CRF}, and maximum clot retraction force CRF_{max} measured by the mHRM provided a set of parameters for us to assess the full complexity of the coagulation system and for global measurement of the hemostasis under different clotting agent and pro- and anti-coagulant treatments.

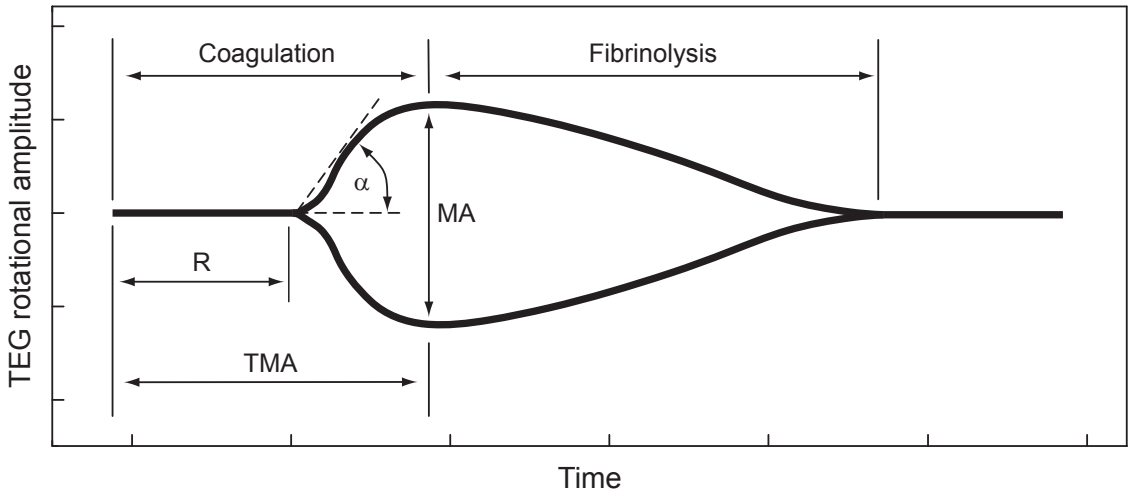

Figure 2.8: Schematic of the TEG tracing plotted with both the dynamic amplitude curve and its mirror as the TEG instrument readout, with key parameters highlighted. TEG tracing showed similar dynamic pattern as that in mHRM, with R correspondent to reaction time T_r, TMA correspondent to time to maximum amplitude T_{max}, α correspondent to CRF growth rate G_{CRF}, and MA correspondent to maximum CRF CRF_{max} in mHRM tracing.

2.3.3 Effect of temperature on clot retraction force

Low body temperature (hypothermia) is known to slow down blood clotting process [39]. To illustrate the utility of the mHRM for blood coagulation tests, we first examined the effect of temperature on clot retraction force development using the mHRM. Blood coagulation was initiated by re-calcification but without supplementation of the clotting factor thrombin. Compared to that at room temperature (25 °C), development of clot retraction force during blood coagulation was significantly expedited at 37 °C, with significantly shortened reaction time T_r and time to maximum amplitude T_{max} (Figure 2.9). Growth rate of clot retraction force G_{CRF} was significantly increased at 37 °C as compared to 25 °C (Figure 2.9a). Specifically, the reaction time T_r, time to maximum amplitude T_{max}, and growth rate of clot retraction force G_{CRF} were 8.70 ± 0.62 min, 22.8 ± 1.59 min, and 3.50 ± 0.59 μN/min, respectively, at 37 °C (Figure 2.9b). While at 25 °C, T_r, T_{max}, and G_{CRF} were 24.63 ± 3.10

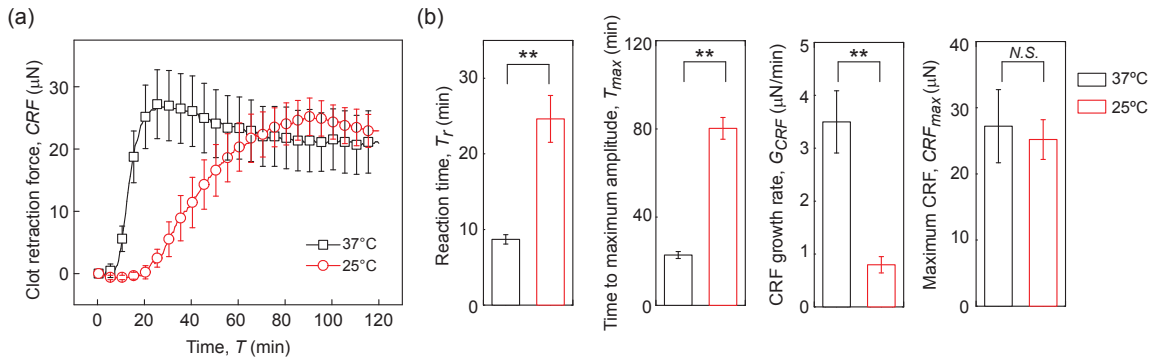

Figure 2.9: Effect of temperature on clot retraction force. (a) Clot retraction force CRF measured by mHRM plotted as a function of time, at both 37 °C and 25 °C. (b) Bar plots of reaction time T_r, time to maximum amplitude T_{max}, CRF growth rate G_{CRF}, and the maximum CRF CRF_{max} as a function of temperature. Data represents mean ± SEM with $n = 4$ at 25 °C and $n = 5$ at 37 °C. **, $P < 0.01$. *N.S.*, $P > 0.05$.

min, 80.25 ± 4.96 min, and 0.80 ± 0.15 μN/min, respectively (Figure 2.9b). Even though the dynamic properties of clot retraction force development appeared sensitive to temperature, the maximum clot retraction force CRF_{max} was not significantly different between 37 °C and 25 °C, with $CRF_{max} = 27.21 \pm 5.53$ μN at 37 °C and $CRF_{max} = 25.19 \pm 3.01$ μN at 25 °C (Figure 2.9b). These temperature-dependent dynamic behaviors were likely the direct effect of different enzyme activity at different temperatures. At 37 °C, coagulation-related enzymes, such as the clotting factors, were more active and thus the coagulation cascade progressed rapidly. In contrast, at 25 °C, these enzymes were less active, so the reaction phase became longer and the CRF also took longer to develop.

2.3.4 Effect of thrombin on clot retraction force

We conducted blood coagulation assays using the mHRM at 25 °C to specifically examine the effect of the clotting factor thrombin on clot retraction force development. After blood re-calcification, 1 μL thrombin (100 U/mL) was added into the blood prior to mHRM measurement. Indeed, compared to re-calcified blood without

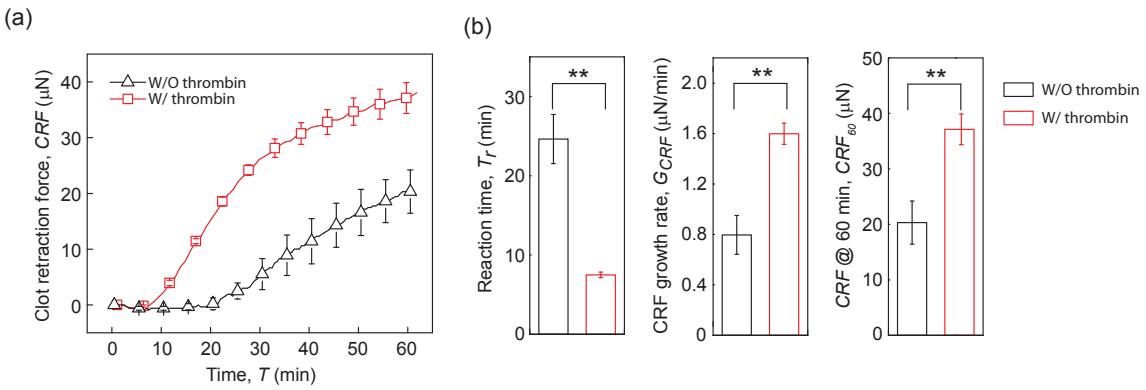

Figure 2.10: Effect of thrombin activation on clot retraction force. All experiments were conducted at 25 °C. (a) Clot retraction force CRF measured by mHRM plotted as a function of time, for blood samples with or without thrombin treatment, as indicated. (b) Bar plots of reaction time T_r, CRF growth rate G_{CRF}, and CRF at 60 min (CRF_{60}) as a function of thrombin activation. Data represents mean ± SEM with $n = 6$ (with thrombin) and $n = 4$ (without thrombin). **, $P < 0.01$.

thrombin treatment, thrombin activation resulted in significantly shortened reaction time T_r before the onset of clot retraction force development and greater growth rate of clot retraction force G_{CRF} (Figure 2.10). Specifically, with thrombin treatment, the reaction time T_r and growth rate of clot retraction force G_{CRF} were 7.50 ± 0.34 min and 1.60 ± 0.08 μN/min, respectively, whereas without thrombin activation, T_r and G_{CRF} were 24.63 ± 3.10 mm and 0.80 ± 0.15 μN/min, respectively. One hour after blood re-calcification ($T = 60$ min), the clot retraction force reached a level of 37.12 ± 2.77 μN under thrombin treatment ($CRF_{60} = 37.12 \pm 2.77$ μN), much greater compared to untreated control ($CRF_{60} = 25.19 \pm 3.01$ μN).

2.3.5 Effects of pro- and anti-coagulants on clot retraction force

To demonstrate the effectiveness of the mHRM for rapid assessment of the effects of pro-coagulant and anti-coagulant medications on the global hemostasis response, we conducted comparative studies using the mHRM at 25 °C on blood samples treated with either aprotinin (pro-coagulant; 80 μg/mL) or heparin (anti-coagulant; 8 U/mL).

Blood samples were re-calcified and supplemented with thrombin after treatments with aprotinin or heparin. Aprotinin is a broad-spectrum serine protease inhibitor with significant abilities to inhibit fibrinolysis. It has been used in coronary artery bypass grafting surgery to reduce blood loss and transfusion requirement [40, 41]. As a well-studied anticoagulant, heparin can bind and potentiate antithrombin III, a major inhibitor of thrombin. Thus, treatment of heparin can effectively inhibit blood coagulation [42]. As expected, heparin treatment indeed suppressed blood clotting completely (Figure 2.11a). No clot retraction force was detected by the mHRM during the entire one hour assay period. In fact, blood samples treated by heparin were still in a liquid phase with no gelation observed at the end of the assay. We should also note that heparin-treated blood samples, with their clotting completely suppressed, served as negative control demonstrating that the intrinsic viscoelastic property of blood had minimal effect on inducing displacements of force-sensing beams in the mHRM (Figure 2.11a).

Aprotinin treated blood, in distinct contrast, demonstrated rapid blood clotting and strong clot retraction. The reaction time T_r and growth rate of clot retraction force G_{CRF} for aprotinin treated blood were comparable to blood samples treated with thrombin alone (for aprotinin treated blood, $T_r = 5.00 \pm 2.08$ min, and $G_{CRF} = 1.71 \pm 0.10$ μN/min; for thrombin treated control, $T_r = 7.50 \pm 0.34$ min, and $G_{CRF} = 1.60 \pm 0.08$ μN/min). However, clot retraction force at $T = 60$ min (CRF_{60}) was significantly greater for aprotinin treated blood compared to thrombin treated control ($CRF_{60} = 51.38 \pm 2.70$ μN for aprotinin treated blood, and $CRF_{60} = 37.12 \pm 2.77$ μN for thrombin treated control, Figure 2.11b). This observation was consistent with the functional role of aprotinin in inhibiting fibrinolysis and preserving platelet contractile function during blood clotting.

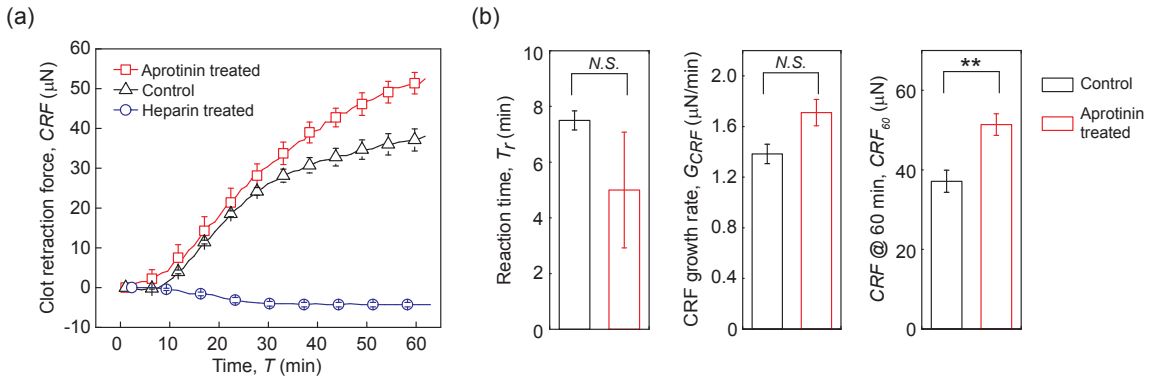

Figure 2.11: Effect of pro- and anti-coagulants on clot retraction force. All experiments were conducted at 25 °C with blood re-calcified and supplemented with thrombin. (a) Clot retraction force CRF measured by mHRM plotted as a function of time, for blood samples pre-treated with aprotinin (pro-coagulant) and heparin (anti-coagulant). Control without any pro- or anti- coagulant treatment was included for comparison. (b) Bar plots of reaction time T_r, CRF growth rate G_{CRF}, and CRF at 60 min (CRF_{60}). Data represents mean ± SEM with $n = 3$ (aprotinin treated), $n = 6$ (control), and $n = 6$ (heparin treated). **, $P < 0.01$. $N.S.$, $P > 0.05$.

2.3.6 Comparison of mHRM with TEG

Coagulation diagnostics using whole blood samples is currently conducted with technologies such as TEG, ROTEM, and HAS. These whole blood coagulation monitoring methods have provided critical information on the major phases of clot formation and lysis. The HAS system is no longer produced. To compare the kinetic signatures of clot retraction force development measured by mHRM with those obtained from TEG, we conducted additional coagulation assays with re- calcified whole blood at both 37 °C and 25 °C using TEG. At 37 °C, clot retraction force measured by mHRM showed very similar dynamics with data obtained from TEG (Figure 2.12a). The reaction time T_r and time to maximum amplitude T_{max} obtained from mHRM were 8.70 ± 0.62 min and 22.8 ± 1.59 min, respectively, comparable with values from TEG, where $T_r = 7.68 \pm 1.07$ min and $T_{max} = 24.28 \pm 2.46$ min (Figure 2.12b). However, at 25 °C, clot retraction force development in the mHRM was significantly

slower than blood clotting in TEG (Figure 2.12c & d). Specifically, reaction time T_r and time to maximum amplitude T_{max} in the mHRM were 24.63 ± 3.10 min and 80.25 ± 4.96 min, respectively, while in TEG, T_r and T_{max} were only 9.22 ± 1.92 min and 32.92 ± 2.07 min, respectively. Slower clot retraction force development in the mHRM at 25 °C when compared to TEG might be attributed to the shear applied to clotting blood in the TEG. It has been well reported in the literature that fluid shear can increase platelet adhesion, aggregation, and thus activation. Applying quasi-static Couette flow model to TEG experimental setup, the shear rate in TEG was estimated to be about 0.2 s^{-1}, which might be sufficient for eliciting platelet activation [43–45]. A higher temperature at 37 °C might lead to expedited biochemical reactions in the coagulation cascade, masking the effect of shear stress on promoting blood coagulation.

2.3.7 Future development for point-of-care testing

Blood coagulation assays for point-of-care applications will require such assays to be fast, robust, yet easy to operate. In its current form, measurements of clot retraction force by the mHRM take about tens of minutes, which is still suboptimal for point-of-care applications. A potential solution to expedite blood coagulation in the mHRM will be to supplement coagulation activators, such as kaolin, into blood samples, as has been commonly conducted in TEG. Specifically, kaolin can significantly shorten the reaction time T_r and increase the clot retraction force growth rate G_{CRF} during blood clotting [46].

Currently, the mHRM requires optical microscopy for image collection. Future effort will be devoted to develop a small diagnostic accessory - a “dongle” - that attaches to a smartphone and has the capability for automatic blood sample loading and precise temperature control. Blood coagulation assays can be run automatically by the dongle on a disposable plastic cassette with preloaded reagents, with results

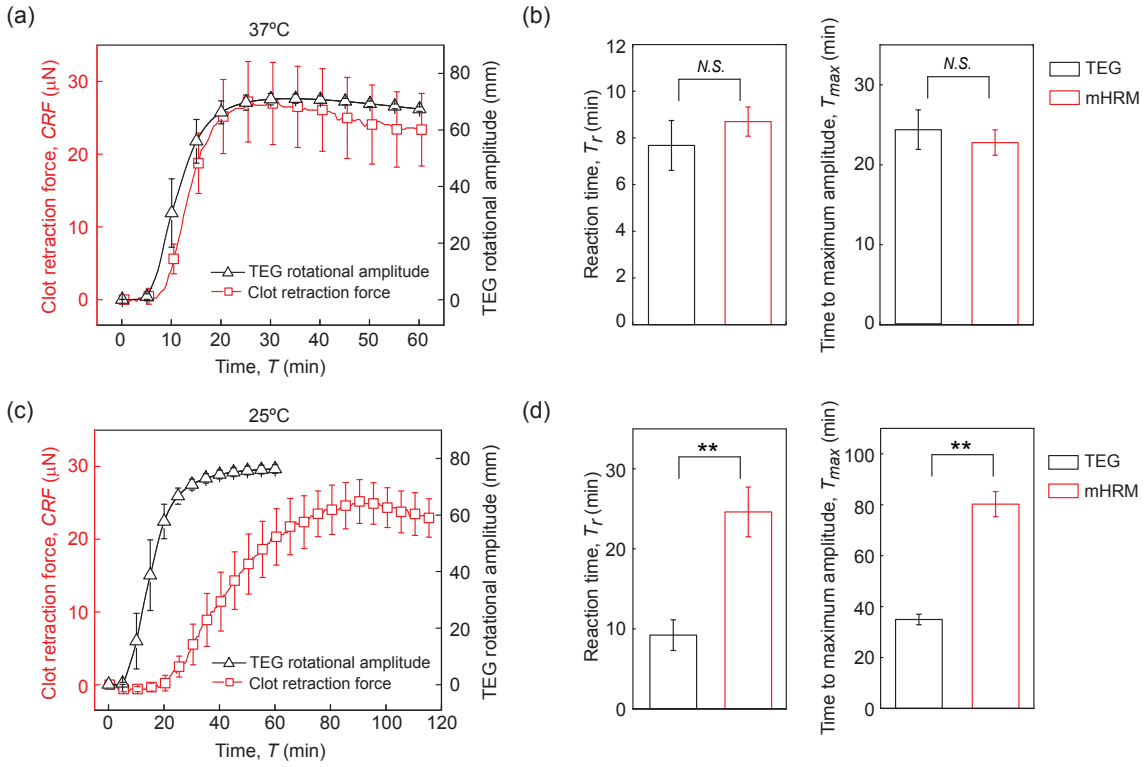

Figure 2.12: Comparison of mHRM and TEG for blood clotting tests at both 37 °C (a & b) and 25 °C (c & d). (a & c) Clot retraction force CRF measured by mHRM and TEG rotational amplitude plotted as a function of assay time, at both 37 °C (a) and 25 °C (c). (b & d) Comparison of reaction time T_r (left) and time to maximum amplitude T_{max} (right) measured by mHRM and TEG at both 37 °C (b) and 25 °C (d), as indicated. Data represents the mean ± SEM with $n = 5$. **, $P < 0.01$. $N.S.$, $P > 0.05$.

captured by smartphone camera and processed simultaneously by the smartphone. We envision that coupling the mHRM technology with recent advances in consumer electronics will lead to the convenience of obtaining quick whole blood coagulation diagnostics results with a single fingerprick, making the existing laboratory-based coagulation diagnostics accessible at home and to almost any population with access to smartphones.

Precise metering of blood sample is critical for accurate measurements of blood coagulation properties. In point-of-care testing using the mHRM, we envision blood sampling to be performed through finger prick in conjunction with a capillary tube that is coupled with a syringe-like dispenser. When blood has been collected in the capillary tube, the dispenser will be connected to the capillary tube and discharge a precise amount of blood onto force sensing elements of the mHRM. Due to hydrophobicity of PDMS and surface tension, blood drops with a prescribed volume will acquire the same shape and position as long as they are properly suspended between force sensing beams in the mHRM.

2.4 Conclusion

The coagulation system is a complex biological system, which balances coagulation and fibrinolysis in an effort to maintain both blood flow and hemostasis. In addition to the acellular (clotting proteins) and cellular (red blood cells, platelets, white blood cells) components of the coagulation system, it is now appreciated that coagulation is also affected by inflammation, tissue oxygenation, and endothelial cell function. There is a growing trend in using technologies to examine blood coagulation to monitor standard coagulation therapies in both thrombolic and hemophilic diseases as well as for diagnostic and therapeutic purposes to guide transfusion therapy and treatments for sepsis, traumatic brain injury, and other acute diseases. Coagulation monitoring technologies using whole blood samples such as TEG and ROTEM are

now becoming increasingly common because unlike traditional PT and aPTT tests, which examine only the protein portion of the blood, TEG and ROTEM examine both cellular and acellular components involved in blood coagulation and can thus provide a more complete picture of the interactions between the coagulation and inflammatory systems. However, despite the important clinical values that TEG-like technologies can bring, existing whole blood coagulation assays share some critical limitations (such as high cost, limited sample throughput, large footprint, etc.) that have rendered them suboptimal for point-of-care applications. In this chapter, I have successfully developed a miniaturized clot retraction assay device termed Miniaturized Hemoretractometer (mHRM) using soft elastic material PDMS and replica molding. Doubly-clamped flexible PDMS beams were incorporated into the mHRM design to serve as mechanical strain sensors to report clot retraction force development during blood clotting. Importantly, kinetic curves of clot retraction force obtained by the mHRM have demonstrated different major phases of clot formation (including the reaction phase, contraction development phase, and fibrinolysis phase), consistent with TEG/ROTEM. Key blood clotting parameters including reaction time T_r, time to maximum clot retraction force T_{max}, clot retraction force growth rate G_{CRF}, and maximum clot retraction force CRF_{max} can be conveniently determined by the mHRM, allowing full assessment of the complexity of the coagulation system and for global measurement of the hemostasis. To demonstrate its clinical utility, the mHRM was utilized for clot retraction force measurements of whole blood samples under different assay temperature, different clotting agent (i.e., thrombin), and pro- (i.e., aprotinin) and anti-coagulant (i.e., heparin) treatments. This preliminary effort demonstrated the ability of the mHRM to detect changes in coagulation consistent with those expected when blood was exposed to various pro- and anti-coagulant medications. This lays the foundation to identify novel signatures of blood clotting dynamics under perturbations to different coagulation components, which will allow

tailoring of specific coagulation tests and treatments to different clinical applications in the future. The mHRM's low fabrication cost, small size, and consumption of only minute amounts of blood samples make the technology promising as a point-of-care tool for coagulation monitoring.

CHAPTER III

Capillary assisted deposition of carbon nanotube film for strain sensing

This chapter is in part adapted from:

> Li, Zida, Xufeng Xue, Feng Lin, Yize Wang, Kevin Ward, and Jianping Fu. "Capillary assisted deposition of carbon nanotube film for strain sensing." *Applied Physics Letters* 111, no. 17 (2017): 173105.

3.1 Introduction

In the current form of mHRM, data acquisition replies on optical instruments, including back light and camera; it makes data collection cumbersome and hinders mHRM's applications for point-of-care testing. To miniaturize the data acquisition setup of mHRM, a potential method is to incorporate electrical components that are strain-sensitive into the force-sensing beams. Such devices would significantly simply the data acquisition setup and also allow real-time CRF monitoring.

Conventional electronics, which is based on printed circuit boards and silicon wafers, is inherently rigid and lacks flexibility and stretchability. While the mainstream research in conventional electronics has been focused on developing faster and smaller units on planar surfaces, there is an emerging development of stretchable

devices for applications such as wearable electronic devices and health monitoring sensors. The curvy nature of biological objects requires electronics to be stretchable to ensure conformable contact. Such need of stretchability led to the emerging field of stretchable electronics [47].

Two major concepts have been successfully adopted for developments of stretchable electronics. One is to make specially designed thin structures before transferring them onto stretchable substrates such as polymers, forming either wavy or island-bridge structures [48]. Such design minimizes strain in the brittle silicon or metal materials and allows bending and stretching. Successful applications in skin sensor [49], cardiac monitoring [50], etc., have been reported using this approach. The other concept applies new functional materials, oftentimes combined with polymers, to make elastic conductors. Among these new materials, carbon nanotube (CNT) is one of the most commonly used given its exceptional electronic properties. Besides its diverse semiconducting properties as a result of tunable chirality [51], CNT has great electron mobility and thus excellent conductivity. In addition, though single CNT has high Young's modulus, carbon nanotube network shows good stretchability [52].

Direct growth based on chemical vapor deposition (CVD) has been the most common fabrication method of CNT films [53]. Such methods fabricate CNT films with good conductivity; however, they generally require high temperature, which is not compatible with most polymer substrates. Alternatively, solution-based deposition methods are more friendly to polymer substrates, although the conductivity of CNT films is compromised compared to CVD [53].

Many methods based on solution deposition have been proposed, including dip coating[54], contact printing [55], inkjet printing [56], solution precipitation [57], and spray coating [58]. However, these methods are either complicated to implement or not capable of generating desired patterns on substrates. In this chapter, we report

a simple yet convenient method to generate patterns of piezoresistive CNT films on the surfaces of elastic polydimethylsiloxane (PDMS). In particular, micropillar arrays were fabricated on the PDMS surfaces before these surfaces were rendered hydrophilic. After CNT solutions were dispensed onto the PDMS surfaces, capillary action drove the solution evenly onto the surface areas covered with micropillars. Water evaporation left a uniform film of CNT deposited on the PDMS surface, with the shape of the envelope of the micropillar array. The effects of CNT concentration and micropillar gap size on coating uniformity, conductivity, and piezoresistivity of CNT films were studied. Our capillary assisted deposition method of CNT film show the potential of being applied in fabrication of flexible CNT thin films for strain sensing [59], which can be used in motion sensors in stretchable electronics as well as in contraction sensors in biomedical devices.

3.2 Experimental section

3.2.1 Preparation of CNT solution

Carboxyl-functionalized multi-walled carbon nanotubes (Cheap Tubes Inc.) were dispersed in deionized water at a concentration of 5 mg/mL using a probe sonicator (Model VCX130, Sonics & Materials Inc.). Dispersed CNT solutions were then centrifuged at 1000 g for 10 min with resultant supernatants extracted as stock CNT solution for later use. The final CNT concentration in the stock CNT solution was 1.616 ± 0.083 mg/mL, as measured by weighing precipitated CNT after complete water evaporation. The CNT stock solution was diluted to generate CNT solutions of lower concentrations.

3.2.2 Fabrication of micropillar array and CNT film

Square-shaped micropillars were designed with the gap distance between adjacent pillars same as micropillar side, to keep the pillar coverage constant on PDMS surfaces. Unless otherwise noted, both the side of and gap size between micropillars were 100 µm. Micropillar arrays were fabricated using soft lithography. Briefly, a silicon wafer with a negative pattern of the micropillar array was fabricated by photolithography followed by deep reactive ion etching. The pillar height was 51.13 ± 0.55 µm, as measured with a stylus profiler (DektakXT, Bruker Corporation). The silicon wafer was then silanized for 4 hr before spin coating PDMS prepolymer (20:1 base-to-curing agent ratio). Spin coating was performed at 600 rpm for 60 s, resulting in PDMS films with a thickness of 105.0 ± 1.0 µm. The PDMS-coated wafer was then baked at 60 °C overnight before the PDMS film was peeled off. The PDMS film was then treated with oxygen plasma (Model PDC-001, Harrick Plasma) for 3 min to turn the PDMS surface hydrophilic. CNT solution was then dispensed at a corner of the micropillar array, typically at a volume of 2 µL, which then spread over the micropillar array evenly. The PDMS film was then placed in a vacuum chamber to accelerate water evaporation and minimize CNT aggregation.

The micropillar array was designed with a dog-bone-shaped envelope to assist electrical measurements. Electrical resistance was measured with a digital multimeter (Model 34401A, Agilent Technologies), with conductive grease (Model 846, MG Chemicals) applied to both ends of the dog-bone shape to minimize contact resistance. For measurements of electromechanical properties of CNT films, the PDMS film with micropillars was laid on a soft PDMS block (30:1 base-to-curing agent ratio) before the CNT film was deposited. The PDMS block was then laid across a stationary stage and a translation stage mounted on an optical table. Gradual movement of the translation stage led to straining of the PDMS film, with position marks on the translation stage recorded for strain calculation.

Phase contrast images were recorded with an inverted microscope (Zeiss Axio Observer Z1, Carl Zeiss AG), and scanning electron images were taken with a cold field emission scanning electron microscope (SU8000 In-line FE-SEM, Hitachi High-Technologies). Raw CNT samples were prepared by dispersing CNTs in water with vortex, instead of sonication to avoid damaging CNT structures [60], before dispensing the CNT solution on a flat PDMS surface. Other samples were imaged as they were.

3.2.3 Data analysis

To construct grayscale histograms, pixels within the deposited areas in the photographs were extracts in Python, and the grayscale distributions were analyzed. CNT film coverage on PDMS surfaces was analyzed by image processing. Phase contrast images of CNT films were recorded, and regions within channels were cropped for processing in Adobe Photoshop (Adobe Systems Incorporated). Specifically, cropped images were converted into binary images, turning regions covered by CNT black and otherwise white. Total areas of these two regions were calculated in ImageJ (NIH, USA). Data fitting was performed in Origin (OriginLab Corp.) or Python.

3.3 Results

3.3.1 Micropillar array suppressed coffee ring effect

The PDMS micropillar array had two major effects on deposition of CNT films on PDMS surfaces. First, when CNT solution was dispensed on PDMS surfaces, capillary force facilitated CNT solution spreading and confined CNT solution in the area with micropillars. Such confining effect provided an effective way to pattern the CNT film. Second, the micropillar array restrained the coffee ring effect. Coffee ring effect originates from the compensating flow that keeps the contact line fixed [60], making particle deposition concentrated on the liquid perimeter, as shown in

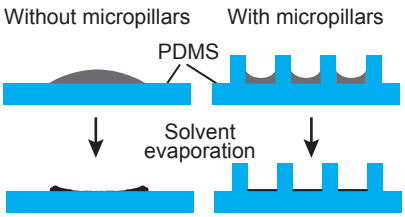

Figure 3.1: Schematic showing capillary assisted deposition of CNT films on PDMS surfaces.

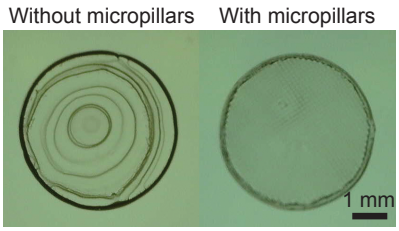

Figure 3.2: Photograph showing CNT deposited on PDMS surfaces without (left) or with (right) micropatterned structures.

Figure 3.1. The micropillar array provided multiple evenly distributed contact lines, suppressing the coffee ring effect and thus leading to a more uniform CNT deposition compared to PDMS surfaces without micropillar arrays (Figure 3.2 & 3.3).

The CNT film deposited on PDMS surfaces with micropillar arrays also showed good uniformity at the microscale, as demonstrated by phase-contrast and scanning electron microscope images (Figure 3.4). Compared to raw CNTs, CNTs were broken up into smaller bundles in the stock solution by sonication during sample preparation (see Experimental section). For example, at a concentration of 0.808 mg/mL, CNTs appeared as individual fibers in contact with neighboring fibers, forming a connected network. The thickness of deposited CNT films was about 40 nm, as measured by the atomic force microscopy (Figure 3.5a).

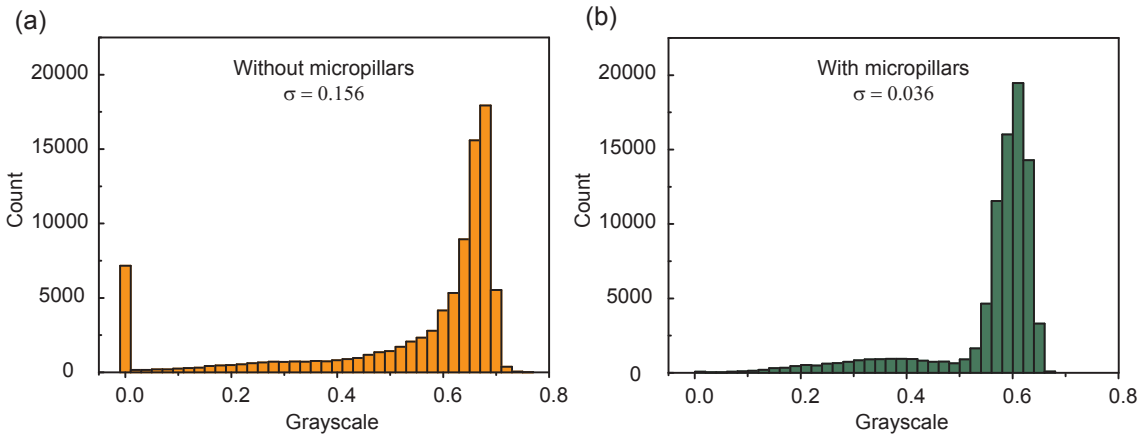

Figure 3.3: Grayscale distributions of the circular areas deposited with CNT in Figure 1b, on PDMS surfaces without micropillars (a) and with micropillars (b). Smaller standard deviation of these histograms suggests a narrower grayscale distribution and thus a more uniform CNT deposition. The standard deviation of grayscale histograms for CNT films deposited on PDMS surfaces with micropillars (0.036) was about one fifth of that without micropillars (0.156).

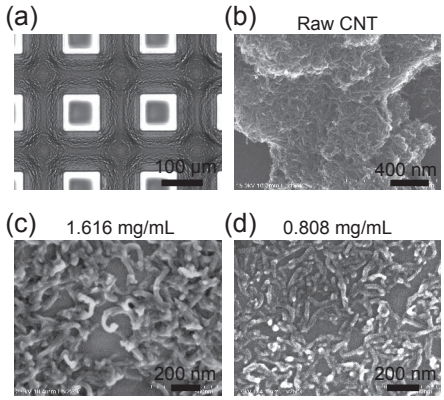

Figure 3.4: (a) Phase-contrast image showing CNT film (1.616 mg/mL) deposited on a PDMS surface with a patterned regular array of squared shaped pillars. (b-d) SEM images show unprocessed CNT materials and CNT films with different concentrations deposited on PDMS surfaces as indicated.

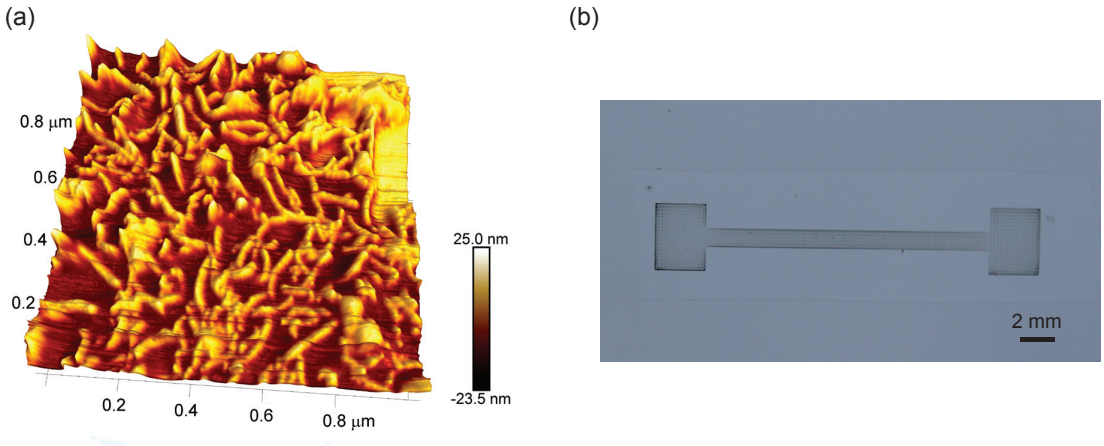

Figure 3.5: (a) Atom force microscope image of the CNT film deposited at 0.808 mg/mL. (b) Photograph of the dog-bone shaped CNT film for resistance measurement.

3.3.2 Conductance of CNT film in agreement with percolation theory

We investigated the conductivity of deposited CNT films and its dependence on CNT concentration. With a CNT concentration of 1.616 mg/mL, the conductivity of CNT film was 11.16 ± 1.23 µS $\cdot$ sq^{-1}. As CNT concentration became lower, CNT film conductivity decreased exponentially (Figure 3.6), consistent with the percolation theory studying through pathways of randomly connected clusters in a random graph [61, 62]. Specifically, our data agreed well with predictions made by the percolation theory that simulates each CNT fiber as a conducting stick (CS), overlapping with other CNTs and forming a connected network. The percolation theory predicts that the conductivity of a two-dimensional film depends on the density of particles following

$$\sigma \propto (N - N_c)^{\alpha} \tag{3.1}$$

where σ is conductivity, N is CS density, N_c is the critical CS density above which percolation happens, and the exponent $\alpha = 1.33$ [61]. The CS density scales linearly

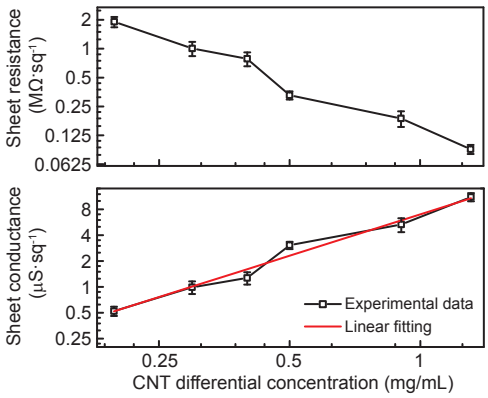

Figure 3.6: Sheet resistance (top) and conductance (bottom) as a function of CNT differential concentration as defined in Equation 3.2.

with CNT concentration, which gives

$$\sigma \propto (\rho - \rho_c)^{\alpha} \tag{3.2}$$

where ρ is CNT concentration and ρ_c is the critical CNT concentration. Fitting of the CNT sheet conductance experimental data using Equation 3.2 gave ρ of 0.308 mg/mL and an exponent α of 1.61, which was close to the theoretical value of 1.33 but somewhat greater. This discrepancy potentially resulted from the fact that CNT films deposited on PDMS surfaces were not perfectly two-dimensional, which was particularly evident at higher CNT concentrations (Figure 3.4c). The percolation theory predicts the critical exponent α of 1.94 for a three-dimensional, randomly connected clusters [61].

3.3.3 Effect of micropillar gap size

Micropillar gap size is a major geometric parameter that affects CNT film deposition on PDMS surfaces, since it directly relates to the contact line number, affecting the extent of coffee ring effect and thus CNT film deposition [60]. We thus sought to determine the micropillar gap size that could result in optimal CNT film deposition.

Here, we define CNT film surface coverage as the ratio of areas covered with CNT to the total area of the channel bottom. As shown in Figure 3.7a & b, micropillar arrays with a gap size of 80 µm and 150 µm had a high surface coverage of $79.3 \pm 1.0\%$ and $76.4 \pm 2.4\%$ by CNT films, respectively. When the micropillar gap size became smaller or larger out of this range, deposited CNT films became less uniform with less surface areas covered by deposited CNT films. For example, for micropillar gap sizes of 40 µm and 200 µm, the CNT film coverage was $52.1 \pm 7.0\%$ and $58.7 \pm 2.2\%$, respectively. The biphasic effect of micropillar gap size on CNT film coverage was possibly due to multifaceted effects of micropillars on CNT film deposition. The coffee ring effect predicts that solute deposition tends to concentrate around the contact line. As a micropillar array with a smaller gap size has closer contact lines, CNT deposition is supposedly more uniform. However, due to capillary action, CNT solution tends to climb up micropillars and form meniscus, which inevitably results in heightened CNT deposition close to pillar side walls. Thus, the micropillar array with 40 µmgap size had more contacts between CNT solution and pillar walls and thus more meniscus, which potentially led to less uniform CNT deposition on PDMS surfaces.

Sheet conductance of CNT films showed a different dependence on micropillar gap size compared to CNT film coverage (Figure 3.7c). When the micropillar gap size was less than 80 µm, similar as CNT film coverage, the sheet conductance was reduced. For example, the sheet conductance of CNT film with micropillars with 40 µm gaps (5.80 ± 0.77 $\mu S \cdot sq^{-1}$) was about half of that of CNT film with micropillars with 80 µm gaps (10.76 ± 1.20 $\mu S \cdot sq^{-1}$). However, when the micropillar gap was greater than 80 µm, unlike CNT film coverage, the CNT sheet conductance remained roughly unchanged around 12 $\mu S \cdot sq^{-1}$. Specifically, when the micropillar gap size increased from 80 µm to 200 µm, while the CNT film coverage reduced from $79.3 \pm 1.0\%$ to $58.7 \pm 2.2\%$, the sheet conductance became 12.68 ± 1.38 $\mu S \cdot sq^{-1}$, not significantly different from 10.76 ± 1.20 $\mu S \cdot sq^{-1}$ at 80 µm gap size ($P > 0.05$). This was likely

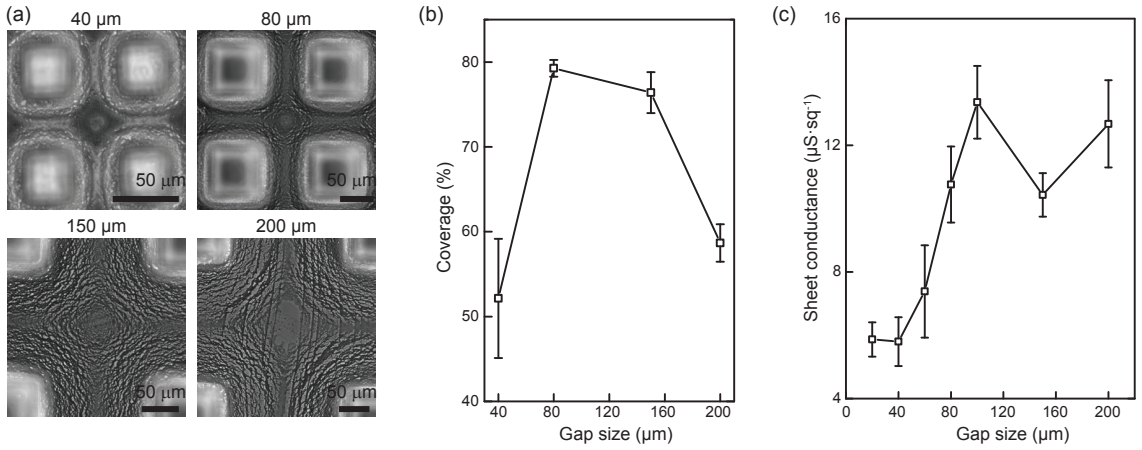

Figure 3.7: Effect of pillar gap size on coating uniformity and conductivity of CNT film. (a) Micrographs of CNT films deposited on PDMS surfaces with micropillar arrays with different gap sizes as indicated. (b & c) Coverage (b) and sheet conductance (c) of CNT films deposited on PDMS surfaces as a function of micropillar gap size.

because at 200 µm, even though CNTs showed more aggregation and the CNT film coverage was reduced, CNT fibers were still connected (Figure 3.7a) and thus the CNT sheet conductance was not significantly affected. In contrast, with 40 µm micropillar gap size, CNT fibers formed discrete islands, rendering the whole CNT film less conductive.

3.3.4 CNT films showed good piezoresistivity

To explore the potential use of deposited CNT films for strain sensing, we specifically measured electromechanical properties of CNT films deposited at different concentrations including their gauge factors. We fabricated CNT films in dog-bone shapes (Figure 3.5b) and applied uniaxial stretch along the axial direction of the bone shape while simultaneously monitoring electrical resistance changes of deposited CNT films. As shown in Figure 3.8, when the CNT concentration was 0.808 mg/mL and 1.212 mg/mL, the gauge factor of deposited CNT films increased with applied strain, consistent with previous reports [63]. For example, for CNT concentration of 1.212

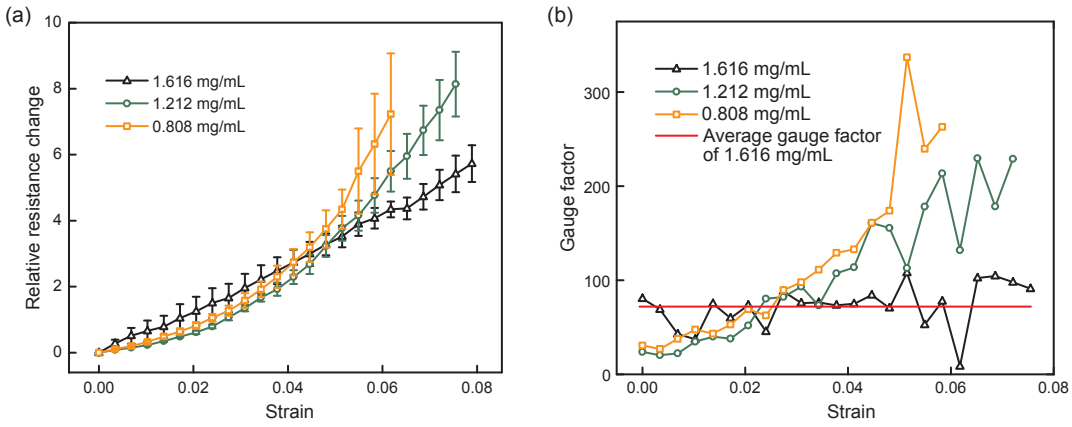

Figure 3.8: Relative resistance change (a) and corresponding gauge factor (b) of CNT films at different CNT concentrations as a function of strain.

mg/mL, the gauge factor of deposited CNT films was 34.7 and 213.6 with a strain of 0.01 and 0.058, respectively (Figure 3.8 b). However, when CNT concentration was increased to 1.616 mg/mL, the relative resistance change of deposited CNT films appeared linearly increasing with applied strain (R^2 = 0.99, data not shown; Figure 3.8a), leading to a relatively constant overall gauge factor of about 71.8 (Figure 3.8b). The linear dependence between relative resistance change and applied strain at this CNT concentration showed the potential of the CNT films for straining sensing applications.

3.4 Conclusion

Carbon nanotube, as an emerging smart functional nanomaterial, has unique electrical properties, rendering them very promising for applications in stretchable electronics. In this work, we report a simple but convenient method for uniform deposition of thin CNT films as strain sensing functional materials on flat PDMS surfaces by fabricating micropillar arrays on the PDMS surfaces and rendering the surfaces hydrophilic through plasma treatments. Owing to capillary forces, CNT solutions dispensed on PDMS surfaces would cover the surfaces uniformly with the shape of

the micropillar array. Importantly, the micropillar array would suppress the coffee ring effect to ensure uniform CNT coating on the PDMS surfaces after water evaporation. We studied different parameters that could affect the quality of CNT film deposition, including CNT concentration and micropillar gap size.

Compared to other solution-based CNT deposition processes such as spray coating, our method does not require stencil for patterning and thus it is more suitable in applications where CNT patterning is desirable. Our method is also compatible with most soft-lithography based fabrication processes, making it easily applicable to other research laboratories. We believe this method will find applications in strain sensing in stretchable electronics as well as contraction force measurements in biomedical researches [64, 65].

CHAPTER IV

The CNT-strain-sensor-based hemoretractometer for blood clot retraction testing

This chapter is in part adapted from:

> Li, Zida, Yize Wang, Xufeng Xue, Brendan McCracken, Kevin Ward, and Jianping Fu. "Carbon Nanotube Strain Sensor Based Hemoretractometer for Blood Coagulation Testing." *ACS Sensors*, DOI: 10.1021/acssensors.7b00971 (2018)

4.1 Introduction

This thesis aims to develop a micro-engineered device for blood clotting assay with the potential of point-of-care applications. Such devices have many merits as compared to conventional blood coagulation assay, such as small device size, low blood consumption, low lost, and high throughput, which could greatly improve patient care and decision making in clinical settings such as perioperative hemostatic monitoring [66], transfusion therapies [67], thrombosis (atrial fibrillation, DVT, PE) treatments [68], hemophilic disease treatments, and treatments for multisystem trauma, sepsis, traumatic brain injury, and other acute diseases [26].

In Chapter 2, I discussed the design of an image-based hemoretractormeter and

demonstrated its utility. The design successfully captured key signatures in coagulation profiles and differentiated blood samples under different drug treatments. Nonetheless, mHRM's data acquisition relied on image capturing using a digital microscope [64]. Such microscopes required certain working distance and a sturdy stand to minimize the vibration during image collection, which could be problematic in a point-of-care testing scenario. To this end, incorporation of electrical units into the PDMS force sensor is beneficial; electrical units generate electrical signal that can be conveniently collected and analyzed by an integrated circuit chip, which significantly reduces the size of the instrumentation. Additionally, replacing digital microscope with IC chips reduces the cost.

Motivated by this concept, in Chapter 3, I developed a method to conveniently coat CNT on PDMS and characterized the piezoresistivity of the resultant CNT films. Results showed that the deposited CNT films had good uniformity and piezoresistivity, which implied their application potential as strain gauges in the development of strain-sensing devices [69].

To further improve mHRM's capability and equip it with electrical readout, in the following work, I implemented the CNT deposition method into the design of mHRM and developed a CNT-based mHRM (CNT-mHRM). In particular, I redesigned the architecture of mHRM: instead of using two protrusions on doubly-clamped beams as in mHRM, I adopted a fixed protrusion and a membrane-like PDMS beam to localize the blood sample (see Figure 4.1a). Using the CNT deposition method I developed in Chapter 3, I successfully fabricated CNT strain sensor on the force-sensing beam and captured beam deformation by monitoring the resistance. I characterized the electromechanical response of the force-sensing beam and optimized the design parameters, including the concentration of the depositing CNT solution and geometry of the force-sensing beam. To validate the results generated by CNT-mHRM, I tested blood samples and conducted measurements based on both resistance and images.

These two measurements generated consistent results, which confirmed the efficacy of CNT-mHRM. By performing assays on blood samples treated with pro- and anti-coagulants, I demonstrated that CNT-mHRM was capable of differentiating blood samples with different coagulation profiles [70]. The CNT-mHRM devices showed great potential for point-of-care blood coagulation testing as an *in vitro* diagnostic device.

4.2 Experimental section

4.2.1 Preparation of CNT solution

CNT solution was prepared as described in Chapter 3. Briefly, carboxyl-functionalized multi-walled carbon nanotubes (Cheap Tubes Inc.) were dispersed in deionized water at a concentration of 5 mg/mL using a probe sonicator (Model VCX130, Sonics & Materials Inc.). Solutions containing dispersed CNT were then centrifuged at 1000 g for 10 min with resultant supernatants extracted as stock CNT solution for later use [71]. The final CNT concentration in the stock CNT solution was 1.616 ± 0.083 mg/mL [69].

4.2.2 Device design and fabrication

The CNT-mHRM device was composed of three layers. The CNT strain sensor resided in the membrane-like, PDMS-made top layer, which was affixed to a rigid acrylic-made middle layer (Figure 4.1a & b). The bottom layer was designed with a protrusion on the center, providing a locus to hold the tested blood sample.

The fabrication of mHRM device involved laser cutting acrylic sheet and replica molding of PDMS. Laser cutting were conducted with a laser cutter system (VLS6.60, Universal Laser Systems). Cutting patterns were designed in AutoCAD (Autodesk, Inc.); laser power and cutting speed were determined from the user manual based on

the thickness of the acrylic sheet with adjustments. Replica molding of PDMS started with mixing PDMS base with curing agent at certain ratios. The mixture was then degassed for about 30 min to remove air bubbles before it was poured on the molds. The molds with PDMS was then degassed again before being baked in 60 °C oven overnight. The cured PDMS was then peeled off from the molds. Base-to- curing agent ratios of 10:1, 15:1, and 20:1 generated PDMS blocks with Young's modulus of 1.717 ± 0.034, 0.615 ± 0.009, 0.301 ± 0.009 MPa, respectively, as measured by Instron tensile testing machine (Illinois Tool Works Inc.).

The middle layer was acrylic shaped by laser cutting. The bottom layer was made of PDMS by replica molding while the mold was also acrylic shaped by laser cutting. The mold consisted of two layers: one layer had hollow rectangle structure, and the other layer had engraved wells. These two layers were cut separately and affixed together before use (Figure 4.2). PDMS base and curing agent mixture (10:1) were then poured into the hollow area and excess PDMS were removed using a blade, before the baking and peel-off step as discussed above.

The top layer featured micropillar arrays to facilitate CNT coating in following steps. The micropillars were in square shape with 100 µm sides and the gap size between adjacent pillars was also 100 µm. The top layer was fabricated by PDMS soft lithography with silicon masters, which were fabricated as described in Chapter 3. Briefly, a silicon wafer was patterned through photolithography and deep reactive ion etching before it was silanized and spin-coated with PDMS base and curing agent mixture. Spin coating was conducted at either 400 rpm or 600 rpm for one minute, generating PDMS membranes with thicknesses of 174.3 ± 4.37 µm or 105.0 ± 1.0 µm, respectively, as measured with a stylus profilometer (Dektak XT, Bruker Corporation). The spin-coated PDMS was then baked and peeled off as aforementioned. Ridges were designed along the beam outline, and a scalpel was used to cut out the beams along the ridges. The length and width of the beams were 15 mm and 2.6 mm

respectively.

The three layers were assembled by chemically bonding acrylic and PDMS layers. Briefly, acrylic surfaces was treated with oxygen plasma (Model PDC-001, Harrick Plasma) for one minute before being immersed in 1% (3-aminopropyl)triethoxysilane (APTES) for one hour and air dried. The PDMS surface was treated with oxygen plasma for one minute before being put in contact with the APTES-functionalized acrylic. The assembly was then baked at 60 °C for one hour to assist chemical bonding [72]. The micropillar arrays were then treated with oxygen plasma for three minute to turn the PDMS surface hydrophilic before CNT solution, typically with a volume of 1.5 µL, was dispensed at a corner of the micropillar array and spread over the micropillar array evenly. The device was then placed in a vacuum chamber to accelerate water evaporation and minimize CNT aggregation [73].

4.2.3 Device characterization

Devices were characterized to obtain the spring constant and gauge constant (see Equation 4.1 & 4.3). As shown in Figure 4.3, a probe force transducer (Model 400A, Aurora Scientific Inc.), which was mounted on a translation stage, was used to measure the force applied. While the probe was approaching and deforming the beam at the center, the force applied was recorded from the force transducer and the displacement was recorded from the translation stage. In the meanwhile, a digital multimeter (Model 34401A, Agilent Technologies) was used to measure the resistance of the CNT resistor. Conductive grease (Model 846, MG Chemicals) was applied on both ends of the CNT resistor to minimize contact resistance.

4.2.4 Data acquisition

Multiplex data acquisition in the blood test was achieved by the coordination between the digital multimeter and an analog switch (Figure 4.1c). The digital mul-

timeter was connected to a computer via a GPIB Instrument Control Device (Model GPIB-USB-HS, National Instruments) and controlled by a LabVIEW program. A multiplexer (CD4051BE, Texas Instruments), controlled by a microcontroller (Arduino Uno, Arduino Company), was used to implement the analog switch circuit. Switch shifting led to transient connection of different devices to the multimeter for resistance measurements. Triggering signals were also sent by the microcontroller to the digital multimeter to synchronize the resistance acquiring and the switch shifting. The duration of a switch cycle was typically a few seconds depending on the amount of devices being tested.

A cartridge was designed to house the devices for multiplex testing. Lead wires were embedded in the cartridge and projected into loading spots for quick device connection. Images were acquired using a digital microscope (Dino-Lite Handheld Digital Microscope, AnMo Electronics Co.).

4.2.5 Blood specimen and coagulation assays

Whole blood was collected from human volunteers into a vacutainer (BD Vacutainer, BD Company) containing 3.2% sodium citrate under an IRB protocol approved by the University of Michigan (HUM00067675: Non-invasive Monitoring of the Critically Ill and Injured Patient). All blood samples were tested within 4 hours after blood collection.

For blood samples treated with pro- or anti-coagulants, aprotinin (80 µg/mL; Sigma-Aldrich Co.) or heparin (8 U/mL; Sigma-Aldrich Co.) were added into blood and incubated for one hour before assaying with CNT-mHRM devices.

At the beginning of the tests, 20 µL blood sample was suspended between the protrusion and PDMS beam using a micropipette, before 1.2 µL $CaCl_2$ (0.2 M, Fisher Scientific) was added into the blood drop with gentle stirring. A petri dish was used to cover the cartridge to alleviate evaporation before resistance acquisition was started.

Image acquisition was also started when applicable.

4.2.6 Data analysis

The original data, which was time series of electrical resistance, was smoothed with a FFT filter using Origin (OriginLab Corp.). The smoothed resistance data was then converted to clot retraction force following Equation 4.4. To obtain key coagulation parameters, including reaction time T_r and growth rate G_{CRF}, CRF data in contraction development phase was fitted to a quadratic function. Specifically, T_r was defined as the time when CRF started to increase from the baseline level ($CRF = 0$) and growth rate G_{CRF} was defined as the CRF growth rate at T_r following Equation 4.5. Two-sample unpaired Student's t-test was performed in Origin for statistical analysis.

An image-processing program was designed and implemented in Python to analyze beam displacements in the captured videos. Briefly, regions of the beam centers were selected and the outlines of the beams were analyzed by edge detection to obtain the displacement of beam centers relative to the original locations. Displacements were then converted to clot retraction force by multiplying the displacements by the spring constant (see Equation 4.1).

4.3 Results

4.3.1 CNT-mHRM device design and data acquisition

The CNT-mHRM consisted of three parts: a structure layer and two support layers (Figure 4.1a & b). The structure layer mainly consisted of a thin PDMS beam featured with micropillar arrays, made from soft lithography (see Experimental section). Owing to the capillary action induced by these micropillars, CNT was uniformly deposited on the PDMS beam [69]. The deposited CNT film possessed

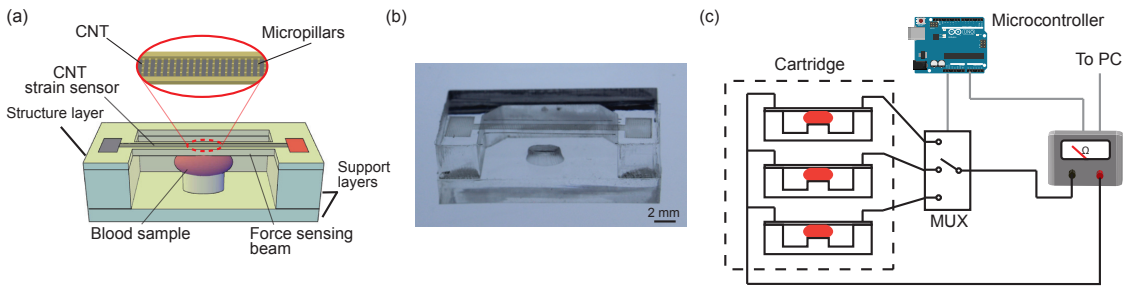

Figure 4.1: (a) Schematic of the CNT-mHRM device. The device was assembled from three parts, with the CNT strain sensor residing on the top PDMS thin beam. The bottom support layer contained a protrusion that held the blood sample along with the PDMS beam. Clot retraction force deformed the PDMS beam, leading to change in the resistance of the CNT strain sensor. (b) Photograph of the CNT-mHRM device. (c) Schematic of the data acquisition setup. The cartridge housed multiple devices, and the multiplexer (MUX) routed the ohmmeters to the device to be measured. Microcontroller coordinated the MUX switching and ohmmeter data acquiring.

good piezoresistivity, making it suitable to serve as a strain sensor. In contact with the PDMS beam layer is a acrylic block, whose Young's modulus is about 2 GPa [74], more than 1000 times stiffer than PDMS. Such high stiffness minimized the PDMS beam deformation induced by factors other than CRF. The bottom support layer was designed with an elliptic cylinder protrusion aligned with the center of the PDMS beam to localize the tested blood sample. The three parts were assembled through plasma bonding (Figure 4.2).

In the blood testing, a drop of citrated blood, typically with a volume of 20 µL, was suspended between the PDMS beam and the elliptical cylinder protrusion by pipetting, before $CaCl_2$ solution was added to the suspended blood drop with gentle mixing. Re-calcification of the blood sample triggered blood coagulation, which induced clot retraction that pulled the PDMS beam and deformed the CNT film. This deformation induced change in the resistance of the CNT strain sensor. By monitoring the resistance of the CNT strain sensor, I could back-calculate the contraction force

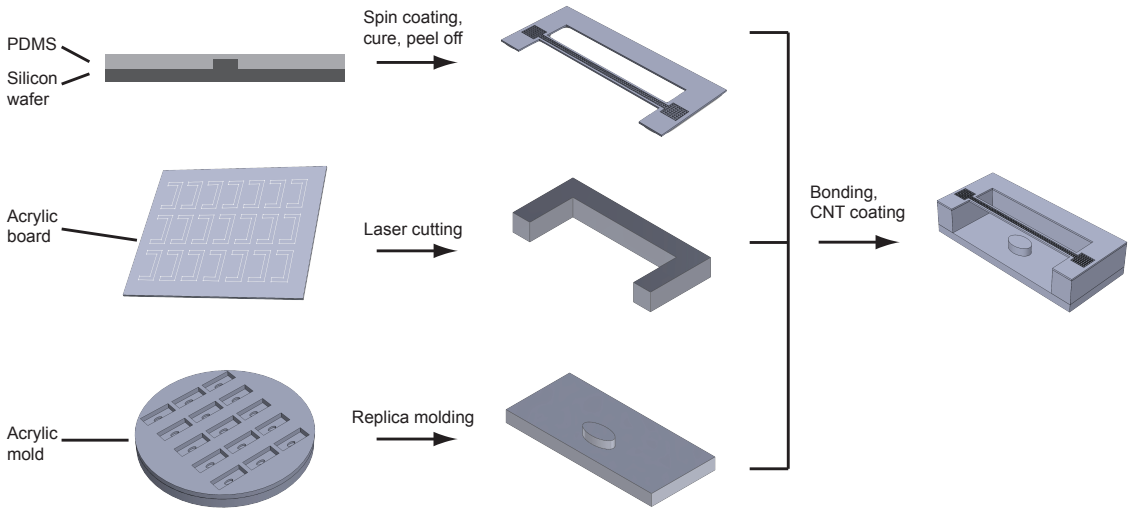

Figure 4.2: Fabrication process of CNT-mHRM devices. The top layer was fabricated by photolithography and soft lithography. The resultant PDMS beam featured with micropillar arrays to assist CNT deposition. Middle layer was made of acrylic through layer cutting. Bottom layer was fabricated by PDMS replica molding. The devices were assembled through plasma bonding.

applied on the PDMS membrane due to clot retraction.

The results of blood coagulation assays are highly dependent on the storage time. The activity of coagulation factors, including factor VIII and factor IX, are gradually reduced after blood collection [75]; platelets undergo activation and depletion of high-energy adenine nucleotide [76]. Thus, high throughput assay is critical to consistent testing results, ensuring that tests are performed within the same time frame after blood collection. To perform multiplex testing, I designed cartridges which was capable of housing up to 10 devices, along with a circuit with an analog switch controlled by a microcontroller (Figure 4.1c). The analog switch routed the multimeter to collect resistance data of a certain CNT-mHRM device at a certain time point. Thus, multiple tests could be performed simultaneously, which greatly improved the test throughput.

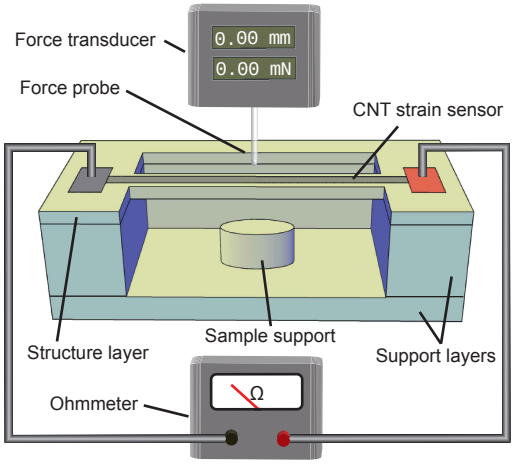

Figure 4.3: Schematic showing the setup of the characterization experiments. A probe transducer, which is mounted on a translation stage (not shown), displaces the center of the beam and measures the force applied. The translation stage records the displacement and a multimeter monitors the resistance.

4.3.2 Device characterization

The contraction force generated by the clot displaces the PDMS beam, leading to change in the resistance of the CNT strain sensor. I designed experiments to characterize the relationship between resistance change of CNT strain sensor and contraction force applied on the PDMS beam, as shown in Figure 4.3. In the characterization experiments, CNT-mHRM devices were fixed on an optical table, and a probe force sensor, which was mounted on a linear translation stage, approached the center of the PDMS beam and displaced it. The force, displacement, and resistance were recorded from the force transducer, translation stage, and multimeter, respectively.

The relationship between the applied force and beam displacement is described by spring constant, which is defined by

$$K = \frac{\mathrm{F}}{\Delta x} \tag{4.1}$$

where K is the spring constant, F is the applied force, and Δx is the displacement. At

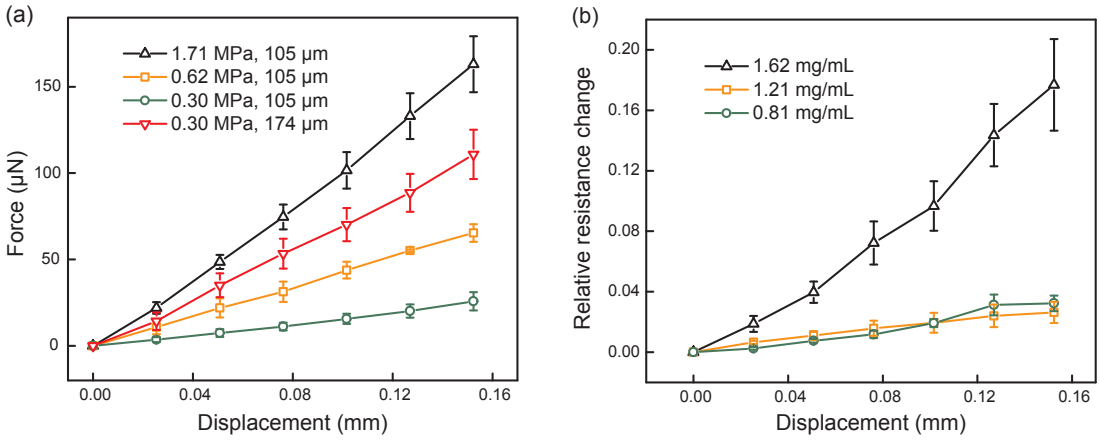

Figure 4.4: Characterization of CNT-mHRM devices. (a) The applied force plotted as a function of displacement of the center of the beams, with beams fabricated using PDMS of different Young's modulus (MPa) and different thickness (μm) as indicated. (b) Relative resistance change plotted as a function of displacement of the center of the beams, with CNT strain sensor fabricated using CNT solutions of different concentrations as indicated.

a given applied force, smaller spring constant leads to greater displacements and thus a higher sensitivity. To achieve good sensitivity, low spring constants are desirable. Classical beam theory predicts that [64]

$$K = \frac{16E\delta^3 W}{L^3} \tag{4.2}$$

where E is the Young's modulus, and δ, W, and L are the beam thickness, width, and length, respectively.

Compared to an ideal beam, beams in CNT-mHRM had more complicated structures such as the micropillar arrays. Nevertheless, Equation 4.2 implied that K is dependent on the Young's modulus of the material and geometry of the beams. Adjusting the ratio of PDMS base to curing agent results in cured PDMS with different Young's modulus and adjusting the spinning speed during spin coating results in PDMS beams with varied thickness (see Experimental section).

I first examined the effect of Young's modulus on the spring constant while main-

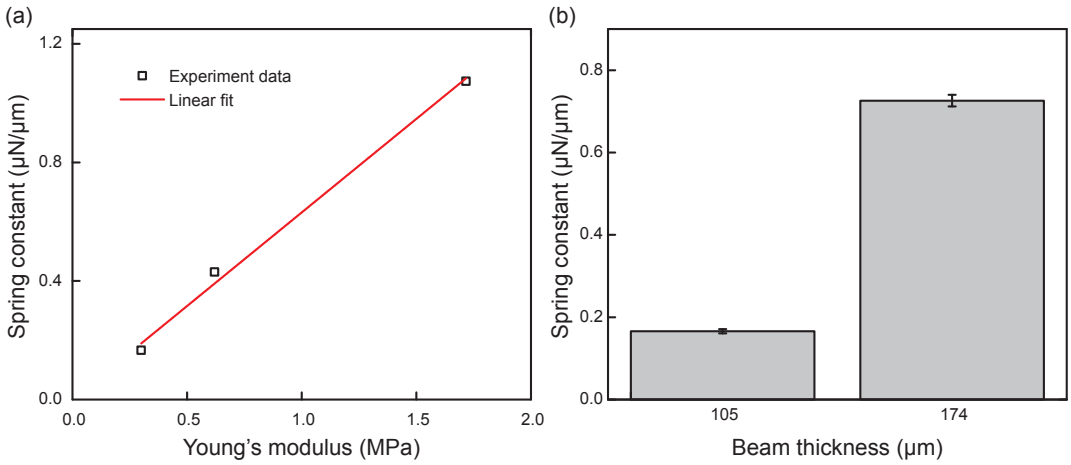

Figure 4.5: (a) Beam spring constant plotted as a function of PDMS's Young's modulus. Spring constant showed strong linear dependence on Young's modulus with a Pearson's correlation coefficient of 0.999. (b) Bar plot of beam spring constant as a function of beam thickness.

taining the thickness of PDMS beams at 105 µm. Results showed that force exhibited linear dependence on beam displacement, with $R^2 > 0.99$ in linear fittings. Results also showed that, as expected, beams fabricated using softer PDMS had lower spring constant. For example, PDMS with Young's modulus of 1.71, 0.62, and 0.3 MPa generated beams with spring constants of 1.074 ± 0.024, 0.430 ± 0.005, and 0.166 ± 0.005 µN/µm, respectively. The relationship between Young's modulus and spring constant showed strong linear correlation, with a Pearson's correlation coefficient of 0.999 (see Figure 4.5a).

Beam thickness is the geometric parameter that can be easily adjusted without redesigning other parts. Thus, I examined the effect of beam thickness on the spring constant of the resultant PDMS beam. Equation 4.2 predicted that thinner beams have lower spring constant, which was also observed in our experimental results. As shown in Figure 4.5b, the spring constant of beams with a thickness of 174 µm was 0.726 ± 0.014 µN/µm, which was about four times of that of beams with a thickness of 105 µm, 0.166 ± 0.005 µN/µm. The lowest thickness was limited by the fabrication

process. When the beam has a thickness lower than 105 µm, it became fragile and very difficult to manipulate.

Relative resistance change responded to beam displacement in a similar manner. As displacement increased, relative resistance change increased accordingly in a linear manner. Similar as spring constant, I define gauge constant (GC) as the ratio of relative resistance change to displacement, following

$$GC = \frac{\Delta R/R_0}{\Delta x} \tag{4.3}$$

where $\Delta R/R_0$ is the relative resistance change and Δx is the displacement.

I characterized the gauge constant of CNT strain sensors deposited using CNT solutions of three different concentrations, namely 0.81, 1.21, and 1.62 mg/mL. The gauge constant at the condition of 1.62 mg/mL was 1.07 ± 0.04 mm^{-1}, which was starkly different compared to that of 0.19 ± 0.01 mm^{-1} and 0.21 ± 0.01 mm^{-1} at the condition of 1.21 mg/mL and 0.81 mg/mL, respectively. The difference between gauge constants of CNT strain sensors deposited at high concentration and low concentration was likely due to the different morphology of the CNT films. As shown in Figure 3.4, CNT film formed a two-dimensional layer when deposited at 0.81 mg/mL, while when deposited at 1.62 mg/mL, the film was thicker and resembled a three-dimensional film. Two-dimensional film and three-dimensional film have been shown to have different electrical properties [61].

Clot retraction force could be deduced from resistance measurements following

$$CRF = \frac{\Delta R}{R_0} \cdot \frac{K}{GC} \tag{4.4}$$

where CRF is clot retraction force, $\Delta R/R_0$ is relative resistance change, K is spring constant, and GC is gauge constant. The ratio of CRF to $\Delta R/R_0$, or K/GC, represents the conversion ratio from relative resistance change to CRF. With a certain

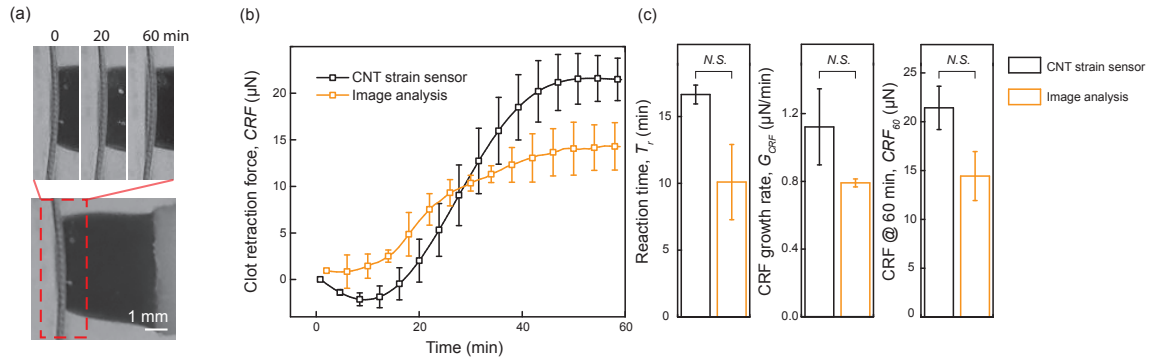

Figure 4.6: Comparison of CRF measured from CNT strain sensors image analysis. (a) Representative micrographs showing the dynamic process of blood clot formation. Scale bar, 1 mm. (b) CRF plotted as a function of time, measured from CNT strain sensor and image analysis, respectively. (c) Bar plots of reaction time T_r, growth rate G_{CRF}, and CRF_{60} of CRF dynamics measured with different methods. Data represents mean ± SEM with $n = 3$. *N.S.*, $P > 0.05$.

precision in resistance measurement, the smaller K/GC is, the smaller the minimum detectable CRF is, and the better the sensitivity is. Thus, low spring constant combined with a high gauge constant generated CNT strain sensors with good sensitivity. Specifically, I chose beams fabricated from PDMS with a Young's modulus of 0.30 MPa and a thickness of 105 μm, and CNT strain sensors deposited using CNT solution with a concentration of 1.62 mg/mL. This combination generated CNT strain sensors with sensitivity of 155.1 μN (per unit resistance change).

4.3.3 Comparison of CNT-mHRM with image analysis

I performed blood coagulation assays using CNT-mHRM devices while simultaneously capturing images of the beams, aiming to validate the force measurements from CNT-mHRM devices. The captured images provided a way to visually monitor the blood coagulation process as well as to calculate clot retraction force: by analyzing the beam displacements in the images, clot retraction force could be calculated following Equation 4.1. Clot retraction forces measured from CNT strain sensor were

calculated following Equation 4.4 using the spring constant and gauge constant that were characterized.

As expected, CNT-mHRM devices captured dynamic clot retraction (Figure 4.6 a) and revealed two major CRF development phases, namely reaction phase and contraction development phase (Figure 4.6b), similar as the original mHRM devices (Figure 2.6 & 2.7) and TEG (Figure 2.8). From the onset of the assay ($T = 0$) to the end of reaction phase ($T = T_r$; designated as reaction time), the coagulation cascade was in process until fibrin network was formed and activated platelets started interacting with fibrin and contracting, leading to rapid increase of CRF in the second phase, contraction development phase. I defined growth rate of CRF G_{CRF} and CRF at 60 min CRF_{60} as

$$G_{CRF} = \left.\frac{dCRF}{dT}\right|_{T=T_r} \tag{4.5}$$

$$CRF_{60} = CRF|_{T=60\ \text{min}} \tag{4.6}$$

The reaction time T_r, CRF growth rate G_{CRF}, and CRF at 60 min CRF_{60} provided a set of parameters to assess the coagulation profiles.

CNT-mHRM generated results that were close to those calculated from beam displacements based on image analysis. The reaction time T_r, CRF growth rate G_{CRF}, and CRF at 60 min CRF_{60} from CNT-mHRM measurements were 16.64 ± 0.71 min, 1.12 ± 0.22 µN/min, and 21.42 ± 2.22 µN, respectively, which were not significantly different compared to 10.09 ± 2.81 min, 0.79 ± 0.02 µN/min, and 14.43 ± 2.50 µN from image analysis, respectively. However, relatively large discrepancy between means of these two measurements were observed. This discrepancy was potentially due to that in addition to contraction force that bent the beams, clots also applied force that was tangential to the beam surface, which could have additional effect on the resistance

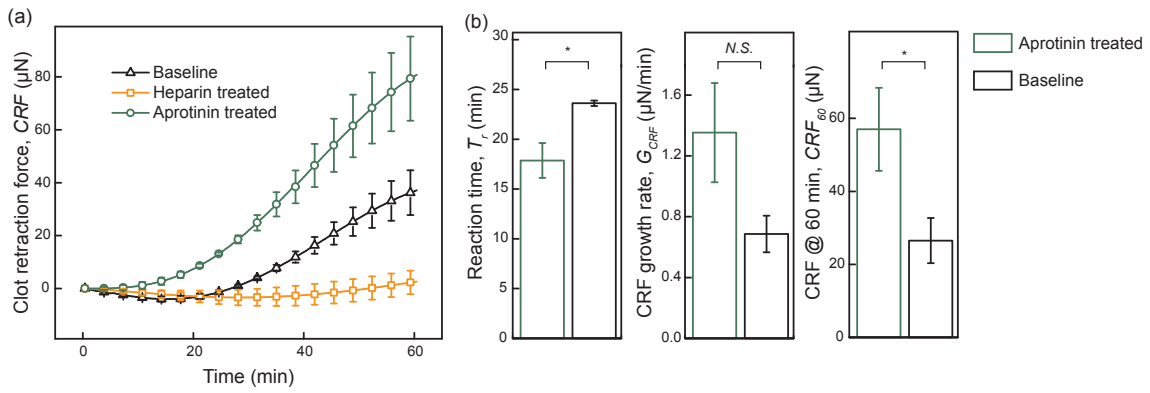

Figure 4.7: Effect of pro- and anti-coagulant on CRF measurements using CNT-mHRM devices. (a) CRF plotted as a function of time, from baseline, heparin-treated, and aprotinin-treated blood samples. (b) Bar plots of reaction time T_r, growth rate G_{CRF}, and CRF_{60} of CRF dynamics measured from aprotinin-treated and baseline blood samples. Data represents mean ± SEM with $n = 3$. *, $P < 0.05$. *N.S.*, $P > 0.05$.

[32].

4.3.4 Effect of pro- and anti-coagulants on clot retraction force

To demonstrate the utility of CNT-mHRM as a diagnostic tool for blood coagulation testing, I conducted experiments using blood samples treated with either pro-coagulant, namely aprotinin, or anti-cogulant, namely heparin. Aprotinin is an inhibitor of several serine proteases such as trypsin and plasmin and thus inhibits fibrinolysis. It has been used in coronary artery bypass grafting surgery to reduce blood loss, transfusion need, and end-organ damage due to hypotension [77]. Blood under the effect of aprotinin has been shown to possess elevated clot retraction force [78]. Heparin is a glycosaminoglycan, which binds to thrombin inhibitor, antithrombin, and increases its inhibition activity by more than 1000 folds [79]. It has been widely used as anti-coagulant (blood thinner) to treat and prevent thrombosis. Treatment of of heparin can greatly inhibit blood coagulation [42].

As shown in Figure 4.7, CNT-mHRM devices captured distinctively different clot

retraction force dynamics from baseline, aprotinin-treated, and heparin-treated blood samples. With blood samples treated with heparin, no detectable contraction force was captured in the assay duration of 60 min, which was consistent with heparin's anti- coagulant funtion. Compared to baseline blood samples, aprotinin-treated blood samples exhibited slight accelerated CRF development and elevated CRF at the end of the assay (60 min). The reaction time T_r from aprotinin-treated blood samples was 17.86 ± 1.75 min, which was significantly less than that of 23.61 ± 0.28 min from baseline blood samples. The CRF at 60 min CRF_{60} were 57.00 ± 11.38 µN, which was about two folds of that of 26.51 ± 6.19 µN from baseline blood samples. Though the growth rates among the aprotinin-treated group and baseline group, which were $1.35 \pm$ 0.33 µN/min and 0.66 ± 0.12 µN/min, respectively, were not significantly different, the three parameters combined together showed CNT-mHRM devices' capability of differentiating treated blood samples from baseline samples.

4.4 Conclusion

In this chapter, I integrated CNT strain sensors into the mHRM beams and developed a new device, named CNT-mHRM, for real-time, high throughput blood coagulation testing. This device consisted of a thin, flexible PDMS beam for force sensing and a fixed protrusion to localize blood samples. CNT strain sensor was fabricated on top of the PDMS beam which reported the generated blood contraction force based on the change in the resistance. I characterized the spring constant and gauge constant of the devices, and performed assays on blood samples. CNT-mHRM generated measurements that were consistent with those calculated from image analysis. I further demonstrated the utility of CNT-mHRM by performing assays on blood samples treated with drugs with known effects. The measurements were consistent with reported results, which showed the capability of CNT-mHRM of differentiating blood samples of different conditions. The small size, low cost, and real time measurement

equipped CNT-mHRM great potential as a point-of-care tool for blood coagulation testing.

It was also noticed that CNT-mHRM generated results with large variations. A few factors could have contributed to these variations. First, the fabrication process involved a few manual steps, such as beam edge cutting and parts alignment, which inevitably introduced device-to-device variations. By the optimizing the process, such as replacing manual cutting with laser cutting and adding markers to assist alignment, the variation in device fabrication would be minimized. Second, in the current form of CNT-mHRM, the CNT strain sensor is exposed to the environment. Disturbance from the environment, such as air flowing and temperature fluctuation, could affect the resistance of the CNT strain sensor [80, 81]. By packaging the CNT strain sensor with an additional layer, this fluctuation effect could be alleviated. Future work should be devoted to address these limitations and enhance the strain sensor performance.

CHAPTER V

Conclusions, perspectives, and future directions

5.1 Conclusions

Perioperative monitoring of blood coagulation is critical for understanding the causes of hemorrhage, to guide hemostatic therapies, and to predict the risk of bleeding during consecutive anesthetic or surgical procedures. There is a growing need to apply technologies to examine blood coagulation. New coagulation diagnostics that use whole blood samples such as thromboelastography (TEG) are becoming a standard of care because unlike traditional prothrombin time assays which examine only the protein portion of blood clotting, TEG utilizes whole blood and can thus provide a more realistic picture of the interaction between coagulation and inflammatory systems. Technologies like TEG provide information on the onset of clotting, strength of clots formed, and how fast clots lyse. Despite the new value that TEG-like technologies bring, the mechanics of such devices require a large footprint, are prone to user error, require large blood volumes, and cannot be used for point-of-care testing. Development of new functional coagulation test platforms which provide similar information but require less blood, footprint, and operator intervention can disrupt a growing market and move such blood test system into the home.

This dissertation focuses on developing a platform for blood coagulation assays with the potential for point-of-care application. Compared to conventional and re-

cently published microfluidic coagulation assay platforms, the designs in this thesis aimed to possess greater potential for commercialization and be readily used by clinical professionals in hospitals and even patients at home. Specifically, it possessed merits including ease of operation, small size, small consumption of blood sample, low fabrication cost, and high throughput.

In Chapter 2, I designed a miniaturized device to assess blood coagulation functionality by measuring the clot retraction force. Clot retraction force is generated during blood clotting and it reflects both the functionality of cellular and acellular components involved in blood coagulation. By measuring this parameter, this device would capture intrinsic information about coagulation functionality. I adopted two doubly-clamped beams made from soft materials (polydimethylsiloxane; PDMS) serving as force sensors, with protrusions at beam centers to hold blood samples. When the blood sample was suspended between the two protrusions, hydrophobicity of the beam material and surface tension ensured that the blood sample acquired a certain shape. This unique design allowed highly reproducible localization of the blood sample with tiny volume, which was critical for precise measurement. By taking images of the beams and tracking the location of the fiducial markers on them, the contraction forces generated were readily deduced. The efficacy of this design was demonstrated by showing the comparability of the readout with a commercialized instrument (Thromboelastography) and its capability to differentiate blood samples treated with anti- or pro- coagulant drugs.

In Chapter 3, I developed a method to incorporate piezoresistive materials into the beams. The resistance of a piezoresistor changes in response to deformation. By recording the resistance of the resistors in the beams, the deformation of the beams and thus the force generated by the clot can be deduced. Consequently, the image acquisition and processing modules can be removed, which largely simplifies the data acquisition and processing part of the assay. Coupling of PDMS with electrical con-

ductors has been a challenge due to the poor adhesion between PDMS and metals. Carbon nanotube (CNT) has superior conductivity and good compatibility with organic polymers, and thus great potential to be integrated in soft materials. In this chapter, I developed a method to deposit CNT on PDMS beams, forming a resistor that serves as a strain sensor. To obtain a uniform deposition, which is critical for the reproducibility of the measurement, I fabricated micro-patterns on the beams to allow uniform spreading of CNT solution on it. The water then evaporates, leaving a uniform CNT film. This CNT film showed sensitive resistance-strain response, which was suitable for the application as strain sensors.

In Chapter 4, I applied the CNT deposition in the new design of mHRM devices, and developed a new device, named CNT-mHRM, which was capable of reporting clot retraction force based on the CNT strain sensor. The mechanical and electrical properties of CNT-mHRM devices, namely spring constant and gauge constant, were characterized for the optimization of the device design. The CNT-mHRM generated measurements that were consistent with those based on image analysis. The utility of CNT-mHRM devices were demonstrated by showing the capability of differentiating blood samples treated with pro- and anti- coagulant. The CNT-mHRM devices provided real time clot retraction force results from resistance measurements, which minimized the requirement on data collection setup.

CNT-mHRM devices have low cost, small size, small blood consumption, high throughput, and little requirement on instrumentation, making it ideal for point-of-care blood coagulation testing.

5.2 Perspectives and applications

I envision two major applications of CNT-mHRM devices: in clinics as a commercialized point-of-care blood coagulation testing tool and in biomedical research laboratories as a blood coagulation assessment tool.

5.2.1 Commercialization

The overall coagulation market is expected to reach 3.58 billion dollars annually by 2019 [82]. Over 100 million PT and aPTT tests are performed annually. While current TEG/ROTEM market is not fully determined, it is rapidly gaining acceptance in the trauma, sepsis, and cardiovascular surgery markets because of the urgent need to understand the contribution of platelet function in clotting along with the increased teaching and acknowledgement that traditional PT and aPTT testing are not adequate to understand the cellular contributions to blood coagulation. A list of medical and surgical entities where coagulation monitoring using the mHRM technology will be valuable for diagnosis and treatments include but are not limited to: trauma, sepsis, liver disease, thromboembolic disease (stroke, deep venous thrombosis, pulmonary embolism), cardiovascular disease and treatment (acute coronary syndrome, myocardial infarction, cardiomyopathy), and cardiovascular procedures (stents, grafting, cardiovascular assist devices). An increasing number of new oral antithrombotic-anticoagulation medicines are now available for treatment of conditions such as atrial fibrillation and thromboembolic diseases in which PT and aPTT testing provide no value [26]. An increasing body of evidence is demonstrating that whole blood thromboelastography (TEG/ROTEM) is capable of providing diagnostic and therapeutic end-points for a growing number of disease processes and surgical procedures as well as for monitoring new anticoagulation medicines. Both TEG and ROTEM are FDA approved for use in the U.S. and CE approved in Europe. Recently, the United Kingdom's National Institutes for Health and Care Excellence (NICE) which is charge of providing guidance to enhance health in the UK, recommended use of TEG and ROTEM to guide transfusion practices and reported its cost effectiveness.

Despite the increasing body of evidence demonstrating value of whole blood coagulation testing using TEG/ROTEM, there continue to be barriers to wide spread adoption. This includes cost (50-60K/device), expensive upkeep, and the need for

larger sample volumes. This makes the potential for multiplexing (providing specific batteries of coagulation testing) difficult. It also makes using such technology in populations like neonates where blood conservation is extremely important difficult. Operator dependent performance has also been noted including values that can change between technicians. Lastly, the large size of TEG and ROTEM make their ability to serve as true POC test very difficult.

In this thesis, I have demonstrated that our technique of whole blood coagulation testing provides coagulation profiles that are consistent with TEG or ROTEM. Coupled with the design profiled above, our approach is significantly cheaper, requires less blood volume, and is small enough to provide point-of-care or near point-of-care service.

I envision developing a commercial product using the razor-razor blade model. A disposable cartridge containing the mHRM device and non-disposable hardware components with the required electrical readout system will be developed. The base customer of our mHRM technology will include hospitals and other health care facilities where coagulation testing is performed (clinics, hospital wards, ICUs, emergency departments, operating rooms). Another very exciting market that can be exploited will be point-of-care testing for home use (via visiting nurses and a growing paramedicine market), pharmacies, etc., which may allow patients and their care providers to more precisely manage the increasing use of oral platelet inhibitors and anticoagulants. I believe a significant component of our value proposition is the low cost, ease of use, and robust nature of the miniaturized mHRM platform. While our platform is simple, it can easily be expanded to allow for multi-sample testing as well as coagulation pathway testing (using pre-doped cartridges with a variety of inhibitors and activators).

5.2.2 Laboratory use

Given the importance of blood coagulation in clinics, there have been considerable researches pertaining blood coagulation. In these researches, CNT-mHRM could be an important instrument for the assessment of coagulation functionality. I envision the application of CNT-mHRM in the following research topics.

1. The effect of certain physiological conditions on blood coagulation. For example, there have been studies on how metastasis affects blood coagulation based on the hypothesis that circulating tumor cells interplay with platelets during extravasation [83]. Another example is the study of the effect of hemorrhagic shock on blood coagulation [84].

2. Developments of new pro-/anti-coagulants [85] and hemostatic therapies. In such studies, CNT-mHRM could be used to gauge the performance of drugs and therapies.

3. Mechanistic study of blood coagulation cascade. For example, to study how deficiency of certain coagulation factors, such as Factor XII [86], affects blood coagulation profile, CNT- mHRM would be a powerful tool.

5.3 Future research directions

5.3.1 Optimization of device performance

CNT-mHRM devices exhibited noticeable variations in the measurements, which needs be minimized to achieve better reproducibility and repeatability. These variations could potentially come from device-to-device variations as well as suboptimal control over experimental conditions. Future work in the optimization of device performance can be devoted to the following.

5.3.1.1 Optimization of fabrication process

As discussed in Conclusion section of Chapter 4, the fabrication should be optimized to reduce device-to-device variations in device geometry and CNT strain sensor performance.

Fabrication process of the PDMS beams can be improved. In the current process, I used a sharp scalpel to manually cut out the edge of the beams along the ridges designed on the silicon molds. This process inevitably introduced variation in the dimensions of the beams. Occasionally, this manual cutting process generated rough edges, which affected the integrity and the strength of the beams. Laser cutting is proposed to replace manual cutting as a process with less human intervention. The challenge in this process would be the alignment of laser beam with the patterns on the PDMS membrane and the alignment of X-Y axis of the laser system with the orientation of the PDMS membrane before laser cutting. Creative design of alignment markers on the PDMS membrane would be helpful in addressing this problem.

Handling of the PDMS membrane can be difficult, since when the membrane is as thin as 100 µm, it would easily entangle and stick to itself. A potential way to solve this issue is to place a few drops of ethanol on a petri dish before laying the PDMS membrane on it. Ethanol's low surface tension ensures that the PDMS membrane lays on the petri dish without folding. After the ethanol has evaporated, the PDMS sticks on the petri dish without serious wrinkles. This method has been tested.

A potential method to enhance the stability of the CNT strain sensor is to protect the CNT strain sensor from being exposed to the environment. The resistance of CNT is affected by the temperature and humidity of the environment [87]. In addition, the disturbance due to air flowing could also potentially affect the resistance. A few methods have been tested though limited success was achieved. Bonding the top surface of the PDMS beams with another layer of flat PDMS membrane had been tried. Since both layers were very thin, this process was

very difficult to operate. Wrinkles were observed on the PDMS membranes, likely due to the residue stress in the PDMS membranes after bonding. To address this issue, a creative fabrication or assembling method is needed.

5.3.1.2 Integration of MEMS cantilever beam into PDMS beam as an alternative to CNT strain gauge

Semiconductor strain gauges have high gauge factors and high strain sensing sensitivity. The fabrication process of MEMS cantilever beams is also well established [88–90]. By integrating MEMS cantilever beam into the PDMS beam in mHRM, a more consistent and robust strain sensing could potentially be achieved. The most challenging part in this method is to transfer the micro structures fabricated on silicon wafer onto PDMS surface. A reported approach is transfer printing, which requires a lab-made experimental setup and careful adjustment on the operation parameters [91].

5.3.1.3 Improvement on the dispersion of CNT in water

Dispersion of nanoparticles in solvent is a research area with intensive studies. In this thesis, I used carboxyl-functionalized multi-walled CNTs and dispersed them in deionized water through sonication. Though in-depth study of CNT dispersion in water is not the focus of this thesis, a detailed process characterization would lead to a better stability of the CNT/water dispersion and thus a more consistent performance of the CNT strain sensors. The effect of these parameters on CNT dispersion should be investigated: CNT functionalization, sonication power and duration, centrifuge parameters, and storage time of the resultant CNT solutions. The dispersion can be characterized using a Zetasizer tool, which measures the zeta potential (dispersion stability) and particle size distribution.

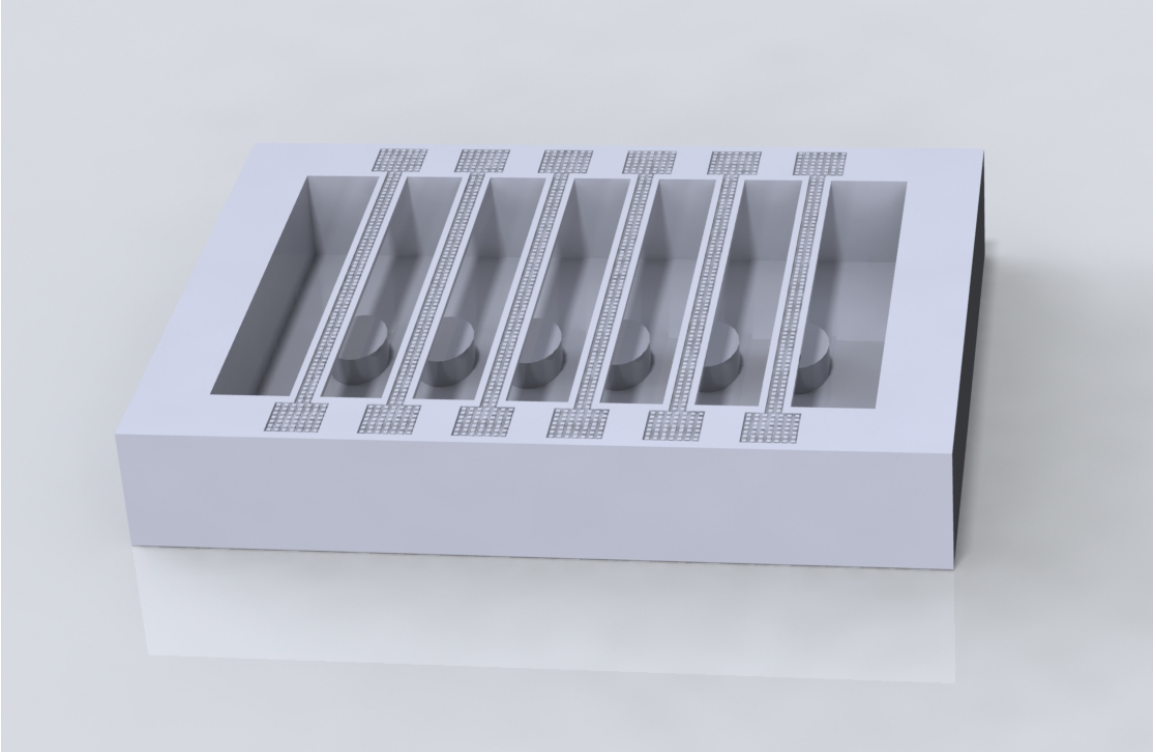

Figure 5.1: Design of a scaled-up CNT-mHRM device. Six beams are integrated in a single device, providing six measurements in each test.

5.3.2 Scale-up

The amount of measurements from a single CNT-mHRM device can be scaled up by incorporating multiple beams, resembling a six-string guitar (see Figure 5.1). This scale-up generates multiple measurements and significantly improves the throughput.

The scaled-up device offers the potential for multiplex testing. By pre-treating the protrusion and/or PDMS beam surfaces with clotting agents, such as kaolin, heparinase, etc., the device can perform a battery of coagulation testing, providing coagulation profiles from different aspects.

5.3.3 Further validation

As a proof of concept, this thesis demonstrated the potential of using mHRM devices for point-of-care blood coagulation testing. Further validation will be necessary

in order to drive mHRM devices to clinics.

Assays using mHRM devices shall be conducted on 70-100 clinical blood samples of patients with wide range of coagulation profiles. For each sample, 7-10 devices shall be tested in order to monitor and document the device-to-device variation. TEG or ROTEM shall be performed simultaneously; these data serve as critical evidences for validation as well as references for device troubleshooting. Well documented data of these tests on clinical samples will also provide insights on the correlation between mHRM measurements and various clinical conditions, which would be useful for future measurement interpretation.

APPENDICES

APPENDIX A

Fabrication protocols of mHRM devices

A.1 Fabrication of acrylic molds

1. Draw cutting lines in AutoCAD (or other similar modeling software). Two files are needed. One file is for the bottom and top layer, and the other file is for the middle layer. Notice that laser cuts out trenches with a width of about 1 mm and normally the resultant shape will be about 1 mm thinner.

2. Laminate a layer of double-sided tape on a 2 mm thick acrylic sheet.

3. Laser cut the acrylic sheet with the AutoCAD files. Cutting speed and power need to be tested. The laser cutter manuals provide reference values for these parameters.

4. Adhere the fabricated acrylic molds on petri dishes.

A.2 Fabrication of the bottom/top layer and the negative molds for middle layer

1. Thoroughly mix PDMS base with curing agent at a weight ratio of 10:1 and degas for about 30 minutes.

2. Pour PDMS base-curing agent mixture into the petri dishes with molds. Place the petri dish in 60 °C oven and bake for at least 6 hours.

3. Peel the cured PDMS off the molds and cut with a blade. The resultant parts out of the molds for bottom/top layer will be used with no further processing. The parts out of the molds for middle layer will serve as the negative molds for the middle layer.

A.3 Fabrication of middle layer

1. Treat the negative mold with oxygen plasma for one minute and silanize it for two hours.

2. Pour PDMS mixture (20:1 base-to-curing agent ratio) on the negative molds.

3. Use a razor blade to scrape on the surface of the negative mold and remove excess PDMS. A degassing process is conducted if there are noticeable air bubbles in the PDMS.

4. Bake the PDMS in 60 °C oven for 6 hours. This baking time is a critical parameter.

5. Peel off the cured PDMS from the negative mold.

A.4 Device Assembling

1. Treat the contacting surfaces of bottom and middle layer with oxygen plasma for one minute.

2. Align and put the two layers in contact and bake in 60 °C oven for five minutes.

3. The top layer is placed on the middle layer before the assay starts. To minimize water evaporation, a thin layer of PDMS base is applied on the side of the top layer before it contacts with middle layer.

APPENDIX B

Fabrication protocols of CNT-mHRM devices

B.1 Preparation of CNT solutions

1. Weigh 50 mg CNTs using weighing paper and high precision balance.
2. Transfer them into a 15 mL conical tube.
3. Add 10 mL deionized water in the tube and shake gentle.
4. Sonicate the mixture with the probe sonicator at 50% power and 50% duty cycle for one hour.
5. Centrifuge at 1000 g for 10 minutes.
6. Extract the top 7 mL for use.

B.2 Fabrication and device assembly

1. Fabricate silicon wafer as discussed in Appendix C.
2. Fabricate bottom layers and middle layers using the same principles as discussed in Appendix A.

3. Treat the middle layer with oxygen plasma for one minute.
4. Immersed the middle layer 1% (3-Aminopropyl)triethoxysilane (APTES) for one hour and air-dry it.
5. Treat the bottom layer with oxygen plasma for one hour.
6. Place the two layers in contact and bake at 60 °C for five minutes.
7. Spin coat 20:1 PDMS base-curing agent mixture onto the patterned silicon wafer at 600 RPM for 60 seconds.
8. Bake at 60 °C for 6 hours.
9. Peel off the PDMS with pattern facing up.
10. Cut out the outline of the beams using a sharp scalpel along the pre-designed ridges.
11. Treat the beams with oxygen plasma for three minute.
12. Pipette 1.5 µL CNT solution onto the micropillar array and place them in a vacuum chamber for one minute.
13. Flip the PDMS beams over and bond them with middle/bottom layer assembly.

APPENDIX C

Fabrication protocols of microstructures on silicon wafer

C.1 Fabrication of photomasks

Film photomasks was ordered from companies, with a minimum feature of 10 µm. When smaller feature sizes were required, chrome photomasks needed to be used instead. The fabrication process of chrome photomasks is described below.

C.1.1 Materials

Glass Mask Plate 5 inches; purchased from LNF store.

(Part Number: *LNF0002*; Mask Plates 5 inches, Soda Lime Glass, 2.29 mm thick, low reflect chrome, AZ1518 Photoresist.)

C.1.2 Processing

1. **Pattern writing on photomasks**

   Initial mask writing uses Heidelberg µPG 501 Mask Maker, following the standard operation protocol provided by LNF. The input file of the pattern drawing

is in .gds format, which can be generated in the open source software of K Layout. A good practice is to design the structures in AutoCAD, convert the structures into a few layered regions, and then import the AutoCAD drawing into K Layout and perform Boolean operations on the regions. Writing time on the mask maker is normally 30 – 60 minutes.

2. **Image reversal and UV exposure (if necessary)**

   When large areas are designed to be transparent, the mask maker writes reverse image on the photomask to minimize the writing time. In this case, an additional step of image reversal followed by UV flood exposure is performed.

   Image reversal uses YES Image Reversal Oven following the standard operation protocols provided by LNF. Make sure to turn the knob of the gas valve to NH_3.

   UV exposure uses MA/BA on Flood Exposure mode for three seconds. A test run using a dummy glass mask is highly recommended.

3. **Development**

   Development uses CEE Developer with the system recipe of *AZ726_5X5_SP_40* when image reversal is not conducted and *AZ726_5X5_SP_20_IR* when image reversal is conducted.

4. **Chrome etching**

   Chrome etching and mask cleaning uses mask bench with the following processes.

   (a) Etch the mask in Chromium Etch Tank for two minutes.

   (b) Rinse the mask in DI Rinse Tank for two cycles.

   (c) Place the mask in Nanostrip for 10 minutes at 60 °C. Make sure to warm up the Nanostrip tank beforehand.

   (d) Rinse the mask in DI Rinse Tank for four cycles.

C.2 Photolithography and reactive ion etching

1. **Photoresist deposition**

   Use ACS200 Cluster Tool with the recipe for thickness of 3.0 µm under the photoresist of SPR 220, following standard operation protocols provided by LNF. HMDS priming is performed automatically by the tool and no extra cleaning step is necessary.

2. **UV exposure**

   Use MA/BA with Hard Contact mode and expose for 12 seconds on film photomask or 10.8 seconds on glass photomask. Detailed operation follows the standard operation protocols provided by LNF.

3. **Development**

   Use ACS200 Cluster Tool with the recipe of *300 DEV 40s* under the entry of Development.

4. **Reactive ion etching**

   Deep reactive ion etching (DRIE) is performed to etch silicon wafers. DRIE uses PEGASUS 4 with the recipe of *LNF Recipe 1*, wherein the etch rate is about 4.5 µm/min. Since the etch rate fluctuates depending on the condition of the tool, a two-step etching is recommended when the feature depth is critical. Underestimate the etch time, run it once, and then measure the depth (see below). With this measured depth, calculate the actual etching rate. Run the etching again with additional etching time.

5. **Depth measurement**

   Use Dektak XT following standard operation protocols provided by LNF.

6. **Photoresist stripping**

The residue photoresist needs to be stripped after etching.

Photoresist stripping uses YES Plasma Stripper with *Recipe 2* following standard operation protocols provided by LNF. *Recipe 2* sets the processing time as 360 seconds. When extra time is necessary, use *Recipe 3* and adjust the processing time as needed.

This concludes the wafer fabrication.

Alternatively, especially when ACS200 Cluster Tool is offline, photolithography is performed with standalone spinners and developers as following.

(a) HMDS priming of wafers

Uses YES Image Reversal Oven with *Recipe 1*. The estimated running time is 15 minutes.

(b) Photoresist deposition

Uses CEE 200 Spinner following standard operation protocols.

(c) Soft bake

Bake at 115 °C for 90 seconds.

(d) Exposure

Same as aforementioned protocol.

(e) Development

Use CEE 200 Developer with recipe *100_mm_DP_40-40*.

BIBLIOGRAPHY

BIBLIOGRAPHY

[1] Nigel Key et al. *Practical hemostasis and thrombosis*. Wiley Online Library, 2009.

[2] Kenichi A Tanaka, Nigel S Key, and Jerrold H Levy. "Blood coagulation: hemostasis and thrombin regulation". In: *Anesthesia & Analgesia* 108.5 (2009), pp. 1433–1446.

[3] Benedicte P Nuyttens et al. "Platelet adhesion to collagen". In: *Thrombosis research* 127 (2011), S26–S29.

[4] Joel S Bennett. "Platelet-Fibrinogen Interactions". In: *Annals of the New York Academy of Sciences* 936.1 (2001), pp. 340–354.

[5] Chauying J Jen and Larry V McIntire. "The structural properties and contractile force of a clot". In: *Cell motility* 2.5 (1982), pp. 445–455.

[6] James G White. "Platelet structure". In: *Platelets* 2 (2007), pp. 45–71.

[7] Eric P Widmaier, Hershel Raff, and Kevin T Strang. *Vander's human physiology*. Vol. 5. McGraw-Hill New York, NY, 2006.

[8] MW Mosesson. "Fibrinogen and fibrin structure and functions". In: *Journal of Thrombosis and Haemostasis* 3.8 (2005), pp. 1894–1904.

[9] Petra Hänecke and Mariam Klouche. "Thrombelastography today: Practicability and analytical power". In: *Transfusion Medicine and Hemotherapy* 34.6 (2007), pp. 421–428.

[10] Alisa S Wolberg. "Thrombin generation and fibrin clot structure". In: *Blood reviews* 21.3 (2007), pp. 131–142.

[11] Dougald M Monroe and Maureane Hoffman. "Theories of blood coagulation: basic concepts and recent updates". In: *Hemostasis and Thrombosis* (2014), pp. 1–13.

[12] Ton Lisman et al. "Hemostasis and thrombosis in patients with liver disease: the ups and downs". In: *Journal of hepatology* 53.2 (2010), pp. 362–371.

[13] T Bombeli and DR Spahn. "Updates in perioperative coagulation: physiology and management of thromboembolism and haemorrhage". In: *British journal of anaesthesia* 93.2 (2004), pp. 275–287.

[14] Paul M Aggeler. "Physiological basis for transfusion therapy in hemorrhagic disorders: a critical review". In: *Transfusion* 1.2 (1961), pp. 71–86.

[15] Myung S Park et al. “Thromboelastography as a better indicator of hypercoagulable state after injury than prothrombin time or activated partial thromboplastin time.” In: *The Journal of trauma* 67.2 (2009), pp. 266–75.

[16] Maureen A McMichael and Stephanie A Smith. “Viscoelastic coagulation testing: technology, applications, and limitations”. In: *Veterinary Clinical Pathology* 40.2 (2011), pp. 140–153.

[17] Alice Chen and Jun Teruya. “Global hemostasis testing thromboelastography: old technology, new applications”. In: *Clinics in laboratory medicine* 29.2 (2009), pp. 391–407.

[18] Marcus E Carr Jr. “Development of platelet contractile force as a research and clinical measure of platelet function”. In: *Cell biochemistry and biophysics* 38.1 (2003), pp. 55–78.

[19] ME Carr Jr. “Measurement of platelet force: the Hemodyne hemostasis analyzer”. In: *Clinical laboratory management review: official publication of the Clinical Laboratory Management Association/CLMA* 9.4 (1995), p. 312.

[20] A Krishnaswarmi et al. “Patients with coronary artery disease who present with chest pain have significantly elevated platelet contractile force”. In: *Thromb Haemostasis* 82.suppl. 1 (1999), p. 162.

[21] Philip E Greilich et al. “Reductions in platelet force development by cardiopulmonary bypass are associated with hemorrhage”. In: *Anesthesia & Analgesia* 80.3 (1995), pp. 459–465.

[22] ME Carr et al. “Batroxobin-induced clots exhibit delayed and reduced platelet contractile force in some patients with clotting factor deficiencies”. In: *Journal of Thrombosis and Haemostasis* 1.2 (2003), pp. 243–249.

[23] ME Carr et al. “Anticoagulant and antiplatelet activities of heparin and low-molecular-weight derivatives”. In: *Blood*. Vol. 82. Wb Saunders Co Independence Square West Curtis Center, Ste 300, Philadelphia, PA 19106-3399, 1993, A603–A603.

[24] ME Carr et al. “Dermatan sulfate suppresses platelet force as it prolongs the APTT”. In: *Blood*. Vol. 88. Wb Saunders Co Independence Square West Curtis Center, Ste 300, Philadelphia, PA 19106-3399, 1996, pp. 3045–3045.

[25] KA McCardell, SL Carr, and ME Carr. “Aprotinin augments protamine sulfate reversal of heparin antiplatelet effects”. In: *Journal of Investigative Medicine*. Vol. 44. Slack Inc 6900 Grove Rd, Thorofare, NJ 08086, 1996, A212–A212.

[26] Michael T Ganter and Christoph K Hofer. “Coagulation monitoring: current techniques and clinical use of viscoelastic point-of-care coagulation devices”. In: *Anesthesia & Analgesia* 106.5 (2008), pp. 1366–1375.

[27] O Cakmak et al. “A cartridge based sensor array platform for multiple coagulation measurements from plasma”. In: *Lab on a Chip* 15.1 (2015), pp. 113–120.

[28] Robert M Judith et al. “Micro-elastometry on whole blood clots using actuated surface-attached posts (ASAPs)”. In: *Lab on a Chip* 15.5 (2015), pp. 1385–1393.

[29] J Berthier et al. “Whole blood spontaneous capillary flow in narrow V-groove microchannels”. In: *Sensors and Actuators B: Chemical* 206 (2015), pp. 258–267.

[30] H Li et al. “Blood coagulation screening using a paper-based microfluidic lateral flow device”. In: *Lab on a Chip* 14.20 (2014), pp. 4035–4041.

[31] Sarah Schwarz Henriques et al. “Force field evolution during human blood platelet activation”. In: *Journal of cell science* 125.16 (2012), pp. 3914–3920.

[32] Xin M Liang et al. “Platelet retraction force measurements using flexible post force sensors”. In: *Lab on a Chip* 10.8 (2010), pp. 991–998.

[33] Shirin Feghhi et al. “E-beam nanopost arrays reveal that glycoprotein Ib–IV–X complex and von Willebrand factor interactions transmit platelet cytoskeletal forces”. In: *ASME 2013 Summer Bioengineering Conference*. American Society of Mechanical Engineers. 2013, V01BT50A004.

[34] Lucas H Ting, Shirin Feghhi, and Nathan J Sniadecki. “Platelet retraction forces induced under high shear gradient activation”. In: *ASME 2013 Summer Bioengineering Conference*. American Society of Mechanical Engineers. 2013, V01BT49A003.

[35] Wilbur A Lam et al. “Mechanics and contraction dynamics of single platelets and implications for clot stiffening”. In: *Nature materials* 10.1 (2011), pp. 61–66.

[36] Xiang Li et al. “Emerging microengineered tools for functional analysis and phenotyping of blood cells”. In: *Trends in biotechnology* 32.11 (2014), pp. 586–594.

[37] Khalil Khanafer et al. “Effects of strain rate, mixing ratio, and stress–strain definition on the mechanical behavior of the polydimethylsiloxane (PDMS) material as related to its biological applications”. In: *Biomedical microdevices* 11.2 (2009), pp. 503–508.

[38] Isaac Cohen and Andre de Vries. “Platelet contractile regulation in an isometric system”. In: *Nature* 246 (1973), pp. 36–37.

[39] Michael J Rohrer and ANITA M NATALE. “Effect of hypothermia on the coagulation cascade”. In: *Critical care medicine* 20.10 (1992), pp. 1402–1405.

[40] W Van Oeveren et al. “Aprotinin protects platelets against the initial effect of cardiopulmonary bypass”. In: *The Journal of thoracic and cardiovascular surgery* 99.5 (1990), pp. 788–96, 788–96.

[41] W Dietrich et al. “Influence of high-dose aprotinin treatment on blood loss and coagulation patterns in open-heart surgery”. In: *Anesthesiology* (1990), pp. 1119–1126.

[42] ME Carr Jr, SL Carr, and PE Greilich. "Heparin ablates force development during platelet mediated clot retraction". In: *Thrombosis and haemostasis* 75.4 (1996), pp. 674–678.

[43] SP Jackson, WS Nesbitt, and E Westein. "Dynamics of platelet thrombus formation". In: *Journal of Thrombosis and Haemostasis* 7.s1 (2009), pp. 17–20.

[44] Jan J Sixma and Philip G Groot. "Regulation of platelet adhesion to the vessel wall". In: *Annals of the New York Academy of Sciences* 714.1 (1994), pp. 190–199.

[45] Warwick S Nesbitt et al. "A shear gradient–dependent platelet aggregation mechanism drives thrombus formation". In: *Nature medicine* 15.6 (2009), pp. 665–673.

[46] Amrita Banerjee, Shauna L Blois, and R Darren Wood. "Comparing citrated native, kaolin-activated, and tissue factor–activated samples and determining intraindividual variability for feline thromboelastography". In: *Journal of veterinary diagnostic investigation* 23.6 (2011), pp. 1109–1113.

[47] John A Rogers, Takao Someya, and Yonggang Huang. "Materials and mechanics for stretchable electronics". In: *Science* 327.5973 (2010), pp. 1603–1607.

[48] Dae-Hyeong Kim et al. "Stretchable and foldable silicon integrated circuits". In: *Science* 320.5875 (2008), pp. 507–511.

[49] Dae-Hyeong Kim et al. "Epidermal electronics". In: *science* 333.6044 (2011), pp. 838–843.

[50] Dae-Hyeong Kim et al. "Materials for multifunctional balloon catheters with capabilities in cardiac electrophysiological mapping and ablation therapy". In: *Nature materials* 10.4 (2011), p. 316.

[51] X Liang. "Transition from tubes to sheets—a comparison of the properties and applications of carbon nanotubes and graphene". In: *Nanotube Superfiber Materials Changing Engineering Design* 1.4 (2014), p. 2.

[52] Darren J Lipomi et al. "Skin-like pressure and strain sensors based on transparent elastic films of carbon nanotubes". In: *Nature nanotechnology* 6.12 (2011), pp. 788–792.

[53] Liangbing Hu, David S Hecht, and George Gruner. "Carbon nanotube thin films: fabrication, properties, and applications". In: *Chemical reviews* 110.10 (2010), pp. 5790–5844.

[54] MH Andrew Ng et al. "Efficient coating of transparent and conductive carbon nanotube thin films on plastic substrates". In: *Nanotechnology* 19.20 (2008), p. 205703.

[55] Yangxin Zhou, Liangbing Hu, and George Grüner. "A method of printing carbon nanotube thin films". In: *Applied physics letters* 88.12 (2006), p. 123109.

[56] Ryan P Tortorich and Jin-Woo Choi. "Inkjet printing of carbon nanotubes". In: *Nanomaterials* 3.3 (2013), pp. 453–468.

[57] Matthew A Meitl et al. “Solution casting and transfer printing single-walled carbon nanotube films”. In: *Nano Letters* 4.9 (2004), pp. 1643–1647.

[58] Erika Artukovic et al. “Transparent and flexible carbon nanotube transistors”. In: *Nano letters* 5.4 (2005), pp. 757–760.

[59] Takeo Yamada et al. “A stretchable carbon nanotube strain sensor for human-motion detection”. In: *Nature nanotechnology* 6.5 (2011), pp. 296–301.

[60] Robert D Deegan et al. “Capillary flow as the cause of ring stains from dried liquid drops”. In: *Nature* 389.6653 (1997), p. 827.

[61] Lea Hu, DS Hecht, and G Grüner. “Percolation in transparent and conducting carbon nanotube networks”. In: *Nano letters* 4.12 (2004), pp. 2513–2517.

[62] GE Pike and CH Seager. “Percolation and conductivity: A computer study. I”. In: *Physical review B* 10.4 (1974), p. 1421.

[63] Yong Li et al. “Piezoresistive effect in carbon nanotube films”. In: *Chinese Science Bulletin* 48.2 (2003), pp. 125–127.

[64] Zida Li et al. “A miniaturized hemoretractometer for blood clot retraction testing”. In: *small* 12.29 (2016), pp. 3926–3934.

[65] Wesley R Legant et al. “Microfabricated tissue gauges to measure and manipulate forces from 3D microtissues”. In: *Proceedings of the National Academy of Sciences* 106.25 (2009), pp. 10097–10102.

[66] Keyvan Karkouti and Kathleen M Dattilo. “Perioperative hemostasis and thrombosis”. In: *Canadian Journal of Anesthesia/Journal canadien d’anesthésie* 53.12 (2006), pp. 1260–1262.

[67] Linda Shore-Lesserson et al. “Thromboelastography-guided transfusion algorithm reduces transfusions in complex cardiac surgery”. In: *Anesthesia & Analgesia* 88.2 (1999), pp. 312–319.

[68] DaLi Feng et al. “Hemostatic state and atrial fibrillation (the Framingham Offspring Study)”. In: *The American journal of cardiology* 87.2 (2001), pp. 168–171.

[69] Zida Li et al. “Capillary assisted deposition of carbon nanotube film for strain sensing”. In: *Applied Physics Letters* 111.17 (2017), p. 173105.

[70] Zida Li et al. “Carbon Nanotube Strain Sensor Based Hemoretractometer for Blood Coagulation Testing”. In: *ACS Sensors* 0.0 (2018). PMID: 29485284, null. DOI: 10.1021/acssensors.7b00971. eprint: https://doi.org/10.1021/acssensors.7b00971. URL: https://doi.org/10.1021/acssensors.7b00971.

[71] Yan Yan Huang and Eugene M Terentjev. “Dispersion of carbon nanotubes: mixing, sonication, stabilization, and composite properties”. In: *Polymers* 4.1 (2012), pp. 275–295.

[72] Vijaya Sunkara et al. “Simple room temperature bonding of thermoplastics and poly (dimethylsiloxane)”. In: *Lab on a Chip* 11.5 (2011), pp. 962–965.

[73] Junrong Yu et al. "Controlling the dispersion of multi-wall carbon nanotubes in aqueous surfactant solution". In: *Carbon* 45.3 (2007), pp. 618–623.

[74] Joel Voldman Carol Livermore. *Material Property Database*. `http://www.mit.edu/~6.777/matprops/pmma.htm`. Accessed: 2017-12-03.

[75] Limin Feng et al. "Effects of storage time and temperature on coagulation tests and factors in fresh plasma". In: *Scientific reports* 4 (2014).

[76] Brian Rosenfeld et al. "Effects of storage time on quantitative and qualitative platelet function after transfusion". In: *Anesthesiology: The Journal of the American Society of Anesthesiologists* 83.6 (1995), pp. 1167–1172.

[77] AM Mahdy and Nigel Robert Webster. "Perioperative systemic haemostatic agents". In: *British Journal of Anaesthesia* 93.6 (2004), pp. 842–858.

[78] Marcus E Carr et al. "Aprotinin counteracts heparin-induced inhibition of platelet contractile force". In: *Thrombosis research* 108.2 (2002), pp. 161–168.

[79] Yung-Jen Chuang et al. "Heparin enhances the specificity of antithrombin for thrombin and factor Xa independent of the reactive center loop sequence evidence for an exosite determinant of factor Xa specificity in heparin-activated antithrombin". In: *Journal of Biological Chemistry* 276.18 (2001), pp. 14961–14971.

[80] Woong Kim et al. "Hysteresis caused by water molecules in carbon nanotube field-effect transistors". In: *Nano Letters* 3.2 (2003), pp. 193–198.

[81] JTW Yeow and JPM She. "Carbon nanotube-enhanced capillary condensation for a capacitive humidity sensor". In: *Nanotechnology* 17.21 (2006), p. 5441.

[82] NA. *Coagulation/Hemostasis Analyzer Market by Product (Clinical Laboratory & PoCT Analyzers), Consumables, Test (PT, Fibrinogen, APTT, ACT, D Dimer, Platelet Function), Technology (Mechanical, Optical, Electrochemical), End User (PoCT) - Forecast to 2021*. Tech. rep. MarketsandMarkets Research Private Ltd., 2016.

[83] David Varon et al. "Involvement of platelet derived microparticles in tumor metastasis and tissue regeneration". In: *Thrombosis research* 130 (2012), S98–S99.

[84] Celeste Harrigan, Charles E Lucas, and Anna M Ledgerwood. "The effect of hemorrhagic shock on the clotting cascade in injured patients." In: *Journal of Trauma and Acute Care Surgery* 29.10 (1989), pp. 1416–1422.

[85] C Male et al. "Recommendations for the development of new anticoagulant drugs for pediatric use: communication from the SSC of the ISTH". In: *Journal of Thrombosis and Haemostasis* 13.3 (2015), pp. 481–484.

[86] Katrin F Nickel et al. "Factor XII as a therapeutic target in thromboembolic and inflammatory diseases". In: *Arteriosclerosis, thrombosis, and vascular biology* (2016), ATVBAHA–116.

[87] Daewoong Jung, Maeum Han, and Gil S Lee. "Humidity-sensing characteristics of multi-walled carbon nanotube sheet". In: *Materials Letters* 122 (2014), pp. 281–284.

[88] YB Gianchandani, CG Wilson, J Park, et al. *Micromachined pressure sensors: Devices, interface circuits, and performance limits*. 2006.

[89] Shwetha Meti, Kirankumar B Balavald, and BG Sheeparmatti. "MEMS piezoresistive pressure sensor: a survey". In: *International Journal of Engineering Research and Applications* 6.4 part 1 (2016), pp. 23–31.

[90] Sandeep Kumar Vashist. "A review of microcantilevers for sensing applications". In: *J. of Nanotechnology* 3 (2007), pp. 1–18.

[91] Matthew A Meitl et al. "Transfer printing by kinetic control of adhesion to an elastomeric stamp". In: *Nature materials* 5.1 (2006), pp. 33–38.